



AFRL-OSR-VA-TR-2014-0254

ULTRATHIN SWCNT FILMS ENABLED MULTI-MODAL FIBER SENSORS

TAO LIU
FLORIDA STATE UNIV TALLAHASSEE

09/30/2014
Final Report

DISTRIBUTION A: Distribution approved for public release.

Air Force Research Laboratory
AF Office Of Scientific Research (AFOSR)/ RTA
Arlington, Virginia 22203
Air Force Materiel Command

REPORT DOCUMENTATION PAGE			Form Approved OMB No. 0704-0188	
Public reporting burden for this collection of information is estimated to average 1 hour per response, including the time for reviewing instructions, searching existing data sources, gathering and maintaining the data needed, and completing and reviewing this collection of information. Send comments regarding this burden estimate or any other aspect of this collection of information, including suggestions for reducing this burden to Department of Defense, Washington Headquarters Services, Directorate for Information Operations and Reports (0704-0188), 1215 Jefferson Davis Highway, Suite 1204, Arlington, VA 22202-4302. Respondents should be aware that notwithstanding any other provision of law, no person shall be subject to any penalty for failing to comply with a collection of information if it does not display a currently valid OMB control number. PLEASE DO NOT RETURN YOUR FORM TO THE ABOVE ADDRESS.				
1. REPORT DATE (DD-MM-YYYY) 19-09-2014		2. REPORT TYPE Final Report		3. DATES COVERED (From - To) July 2011 - September 2014
4. TITLE AND SUBTITLE Ultrathin SWCNT Films Enabled Multi-modal Fiber Sensors		5a. CONTRACT NUMBER		
		5b. GRANT NUMBER FA9550-11-1-0084		
		5c. PROGRAM ELEMENT NUMBER		
6. AUTHOR(S) Liu, Tao		5d. PROJECT NUMBER		
		5e. TASK NUMBER		
		5f. WORK UNIT NUMBER		
7. PERFORMING ORGANIZATION NAME(S) AND ADDRESS(ES) FLORIDA STATE UNIVERSITY, THE SPONSORED RESEARCH SERVICES 874 TRADITIONS WAY TALLAHASSEE FL 32306-0001		8. PERFORMING ORGANIZATION REPORT NUMBER		
9. SPONSORING / MONITORING AGENCY NAME(S) AND ADDRESS(ES) AFOSR WF Role - PK Distribution Air Force Office of Scientific Research 875 North Randolph Street Suite 325, Room 3112		10. SPONSOR/MONITOR'S ACRONYM(S) AFOSR		
		11. SPONSOR/MONITOR'S REPORT NUMBER(S) N/A		
12. DISTRIBUTION / AVAILABILITY STATEMENT Approved for public release; distribution is unlimited.				
13. SUPPLEMENTARY NOTES				
14. ABSTRACT The success of a structure health monitoring (SHM) system for high-performance polymeric composite structures hinges upon noninvasive and embeddable sensors that can be reliably used for sensing the strain, temperature, moisture, irradiation, foreign objects strike damage and other unpredicted events experienced by the host structures. In this project, we developed single-walled carbon nanotube (SWCNT) thin film enabled fiber sensors - SWCNT-FibSen to address this challenge. The fabrication of SWCNT-FibSen is simple, cost-effective, and environmental benign. It can be noninvasively embedded into a polymeric composite structure as a multimodal/multifunction/multipurpose sensor for life-long (from manufacturing to failure) SHM of the host structure. The fundamental research leads to a series of new and reliable methods in characterizing the structures of SWCNTs in the dispersion. This allows for a better understanding of the piezoresistive mechanism(s) of SWCNT thin films and for establishing the processing-structure-property relationships of SWCNT-FibSen sensors. The fundamental and applied research results acquired through this project will pave the way for large-scale production and deployment of SWCNT-FibSen in SHM of polymeric composite structures.				
15. SUBJECT TERMS carbon nanotubes; thin films; Fibers; piezoresistive sensors; embedded sensors; structure health monitoring; polymeric composi				
16. SECURITY CLASSIFICATION OF:			17. LIMITATION OF ABSTRACT UU	18. NUMBER OF PAGES 57
a. REPORT U	b. ABSTRACT U	c. THIS PAGE U		
			19a. NAME OF RESPONSIBLE PERSON Dr. Tao Liu	
			19b. TELEPHONE NUMBER (include area code) 850-410-6606	

Ultrathin SWCNT Films Enabled Multi-modal Fiber Sensors

Final Report (FA9550-11-1-0084)

Prepared by PI: Dr. Tao Liu, Associate Professor

**High-Performance Materials Institute
Department of Industrial and Manufacturing Engineering
FAMU-FSU College of Engineering
Florida State University
Tallahassee, FL 32310**

September 2014

Table of Contents

1. Executive Summary	1
2. Introduction	2
3. Methods and Procedures	4
3.1 Preparation of SWCNT dispersions	4
3.2 Characterization of SWCNT dispersions	5
3.2.1 Spectroscopic Characterization of SWCNT dispersions	5
3.2.2 Sedimentation, Diffusion and Intrinsic Viscosity Measurement of SWCNT dispersions	5
3.2.3 Microscopy examination of SWCNT dispersions	6
3.2.4 Gel Electrophoresis of SWCNTs mapped by Simultaneous Raman scattering and Photoluminescence spectroscopy	6
3.3 Fabrication of SWCNT thin film piezoresistive sensors	7
3.4 Continuous fabrication of SWCNT-FibSen sensors	8
3.5 Fabrication of glass fiber reinforced composite (GFRC) laminates embedded with SWCNT-FibSen sensors	8
3.6 Characterization and Piezoresistivity Evaluation of Various SWCNT sensors	9
4. Results and Discussion	11
4.1 Structural characterizations of SWCNT dispersion	11
4.1.1 Combined intrinsic viscosity, sedimentation and diffusion measurements for determining the length, diameter, molecular mass, mass density and surfactant adsorption	11
4.1.2 Gel Electrophoresis and Raman Mapping for Determining the Length Distribution of SWCNTs	14
4.2 Processing-Structure-Property Relationships of SWCNT thin film Piezoresistive Sensors	18
4.2.1 Effects of film thickness and SWCNT structures	18
4.2.2 Effect of SWCNT orientation	23
4.3 Hybrid approach to tailor the sensing characteristics of SWCNT thin films	28
4.4 SWCNT-FibSen fiber sensors for life-long structural health monitoring of polymeric composites - from manufacturing, utilization to failure	33
4.4.1 Structural characterization of SWCNT-FibSen sensors	33
4.4.2 In-situ resin curing monitoring of polymeric composites	35
4.4.3 In-situ structural health monitoring of polymeric composites -	37
4.4.3.1 Coupled electrical – cyclic tension,	

	bending, and compression tests -----	37
	4.4.3.2 Tension-to-failure test -----	39
	4.4.3.3 Simultaneous tensile tests of multiple SWCNT-FibSen sensors -----	40
	4.5 Graphite nanoplatelet enabled fiber sensor with dual functionalities for realization of multifunctional polymeric composites -----	42
5	Conclusion -----	47
6	References -----	48

1. Executive Summary

The success of a structure health monitoring (SHM) system for high-performance polymeric composite structures hinges upon noninvasive and embeddable sensors that can be reliably used for sensing the strain, temperature, moisture, irradiation, foreign objects strike damage and other unpredicted events experienced by the host structures. In this project, we developed single-walled carbon nanotube (SWCNT) thin film enabled fiber sensors - SWCNT-FibSen to address this challenge. The fabrication of SWCNT-FibSen is simple, cost-effective, and environmental benign. It can be noninvasively embedded into a polymeric composite structure as a multimodal/multifunction/multipurpose sensor for life-long (from manufacturing to failure) SHM of the host structure. The fundamental knowledge acquired on the piezoresistive mechanism(s) of SWCNT thin films allows for establishing the processing-structure-property relationships of SWCNT-FibSen sensors, which will pave the way for their large-scale production and deployment in monitoring the health states of high-performance polymeric composite structures.

The key research achievements for this project are summarized below:

- 1) New and reliable methods were developed in characterizing the structural parameters of SWCNTs in the dispersion – length and length distribution, diameter, defect density, mass density, molecular mass, and surfactant adsorption. This is critical for establishing the processing-structure-property relationships of SWCNT-FibSen and their large-scale production;
- 2) A continuous spray coating and winding process was developed to fabricate SWCNT-FibSen sensors;
- 3) The tailorable sensing characteristics of SWCNT-FibSen have been successfully demonstrate through manipulating the SWCNT structures in the dispersion, forming hybrids with graphite nanoplatelets, controlling the orientation of SWCNTs and selecting different types of fiber substrates, such as glass fiber, polyaramid fiber, nylon fiber, and PET fiber;
- 4) As noninvasive and embedded sensors, the multipurpose sensing capabilities of SWCNT-FibSen for life-long SHM of polymeric composite structure were successfully demonstrated. During the composite manufacturing process, the resin curing can be in-situ monitored by SWCNT-FibSen. After the composite manufacturing process, the same embedded SWCNT-FibSen is capable of detecting/mapping the different mechanical deformation modes - tension, bending, and compression as well as the failure of the host structure;
- 5) By following the similar concept and using the same methods/protocols, we also developed graphite nanoplatelet enabled fiber sensor – GNP-FibSen that can be used as noninvasive and embedded sensors for in situ curing monitoring and structural health monitoring of polymeric composites;
- 6) 10 papers were published in the high-impact journals of the related field, which include Advance Materials, Carbon, Macromolecules, Langmuir, The journal of Physical Chemistry C, RSC Advances, and Macromolecular Chemistry and Physics.

The past three-year research efforts have established a strong foundation, from both the fundamental and applied viewpoints, to prove the feasibility and great potential of using SWCNT-FibSen and GNP-FibSen as the non-invasive, embeddable, and multimodal/multifunction/multipurpose sensors for SHM of high-performance polymeric composite structures. On the pathway to materialize and mature this new technology, we identify the following key issues/needs that should be the subjects for future research and development.

- 1) On the basis of the experimentally established processing-structure-property relationships, simulation and modeling tools need to be developed for better design and optimize the sensing performance of SWCNT-FibSen and GNP-FibSen sensors;
- 2) In the fabrication of SWCNT-FibSen and GNP-FibSen sensors, the final product yield and utilization rate of SWCNT and GNP dispersion need to be improved;
- 3) With a focus on exploring the miniaturized, onboard and wireless sensing devices/systems, the appropriate power and communication schemes for the embedded SWCNT-FibSen and GNP-FibSen need to be developed;
- 4) Appropriate passivating/insulating/packaging methods are needed to protect SWCNT-FibSen and GNP-FibSen to allow their use in the SHM of electrically conducting high-performance polymeric composite structures, e.g., carbon fiber reinforced composites.

2. Introduction

Structural health monitoring (SHM) integrates sensors and sensor networks with structures, e.g., composite aviation vehicles and civil infrastructures, to provide a system-level technology for detection, identification, quantification and decision about their health states [1, 2]. The sensors and sensing system that have been traditionally adopted for SHM applications include metallic strain gage, semiconductor or metal oxide thin or thick films [3, 4], piezoelectric sensors [5, 6], optical fiber sensors [7, 8, 9, 10], eddy-current sensors [11, 12], and magnetostrictive sensors [13]. The recent discovery of the highly sensitive piezoresistivity of carbon nanotubes (CNTs) stimulates great interests in exploring this novel material for developing smart and multifunctional sensors for SHM applications [14, 15, 16]. Very high piezoresistive gauge factors between ~200 to ~3000 have been reported for an individual SWCNT [14, 15, 17]. This property makes individual SWCNTs highly promising for high resolution/sensitivity NEMs strain sensors. However, due to the nanoscale dimension of SWCNTs and their chirality heterogeneity, there have been tremendous difficulties in consistently fabricating individual SWCNT based devices for practical use. To overcome such difficulties, different methods have been proposed in scaling up these nanoscale sensors by using the ensembles of CNTs as the sensing elements. With CNT thin film or buckypaper as the 2-dimensional (2D) sensing elements, the utility of CNTs for strain and corrosion sensing has been demonstrated [18, 19, 20]. In addition, by dispersing CNTs as 3-dimensional (3D) distributed sensing elements, Chou et al. systematically studied their usefulness for damage and failure sensing of glass fiber composites [21, 22, 23]. Using a 1D ensemble structure of CNTs referred to as CNT yarn, Zhao et al [24] and Abot et al [25] both demonstrated the value of CNT based 1D sensing elements as embedded sensors for monitoring the crack initiation and

propagation in composite structures. With glass fiber as substrate, Sebastian et al [26] and Zhang et al [27] respectively applied chemical vapor deposition (CVD) and electrophoretic deposition method to fabricate CNT enabled 1D fiber sensors and explored their application as embedded sensors for damage detection of epoxy matrix or related composites.

Regardless of the sensor type and sensing mechanism(s), some critical characteristics are required for the in-situ or embedded SHM sensors. First, the embedment of SHM sensors must not adversely affect the mechanical properties of the structure being monitored; and the process to incorporate the sensors into the composite structure should be easily implemented and compatible with the manufacturing process of the structure itself. Second, the embedded sensors must be able to survive the pressures and temperatures encountered in the fabrication process of the composite structures, retaining sensing characteristics during the service time of the structure. Third, the sensor fabrication and implementation processes should ensure consistent sensing characteristics for the embedded sensors from one composite structure to another. Fourth, the cost of the SHM sensors and their fabrication should be reasonably low to justify its use for in-situ SHM. This is especially important for wide deployment of an in-situ SHM system, since the number of sensors required in such system may be huge depending upon the size and the desired coverage area of the structure being monitored. For instance, an SHM system of an aerospace vehicle [28, 29] may require 100-1000 sensors. To monitor a small area of delamination, e.g., 5 mm in diameter, requires a sensor network with sensors placed approximately every 50 mm to detect damage [30]. To improve the reliability of a given SHM system by implementing redundant sensors, the number of sensors can be further increased.

As disclosed and discussed in details in this report, we will show that all the above mentioned criteria can be met by a novel 1D sensing element - single-walled carbon nanotube (SWCNT) thin film enabled fiber sensors - SWCNT-FibSen. With a continuous single filament of, e.g., glass fiber, Kevlar fiber, etc., as the substrate (a few tens of μm in diameter), the SWCNT-FibSen sensors were fabricated through a continuous spray coating and winding process. In comparison to the previously developed CNT enabled 1D sensors [24, 25, 26, 27], the fabrication of SWCNT-FibSen is simple, cost-effective, and environmental benign. A typical areal density of SWCNT coating in a SWCNT-FibSen is a few to a few hundreds of $\mu\text{g}/\text{cm}^2$. This makes the materials cost of SWCNT-FibSen very low, even though the raw materials of SWCNTs are quite expensive. Furthermore, the sensing characteristics of SWCNT-FibSen can be tailored through manipulating the SWCNT structures in the dispersion [31], forming hybrids with other types of nanomaterials [32], controlling the SWCNT orientations, and selecting different types of fiber substrates, such as glass fiber, polyaramid fiber, nylon fiber, and PET fiber. Moreover, when embedded into polymeric composites, the SWCNT-FibSen can be used as a multipurpose sensor for life-long (from manufacturing to failure) SHM of the host structure. During the composite manufacturing process, the resin curing can be in-situ monitored by the resistance change of the SWCNT-FibSen. Given its embedded nature, the SWCNT-FibSen provides the resin curing information in the interior of the host composite structure, which cannot be readily accessed by other techniques, e.g., differential scanning calorimetry (DSC) [33]. This is considered a great advantage of SWCNT-FibSen for its use in improving the quality assurance of composite manufacturing process. After the composite manufacturing process, the same embedded SWCNT-FibSen is capable of detecting the different mechanical deformation modes

- tension, bending, and compression as well as the failure of the host structure. The strain/stress mapping can be readily implemented by deploying multiple SWCNT-FibSen sensors at the prescribed orientations and/or locations of the host composite. Last but not least, through a 10,000-cyclic coupled electromechanical test, the embedded SWCNT-FibSen sensor only showed a minor change of the sensor resistance and its piezoresistive sensitivity, which proves the superior robustness of SWCNT-FibSen as the embedded sensors in SHM application.

The large-scale manufacturing and facile deployment capabilities of SWCNT-FibSen sensors as well as their non-invasiveness, robustness, and the ability for in-situ manufacturing process monitoring make SWCNT-FibSen a vantage technique for accurate local damage detection and strain mapping in many complex engineered systems made with lightweight composites, such as a manned or unmanned vehicle airframe or a space satellite optical mirror support. Given the promise of SWCNT-FibSen, its large scale production and deployment requires a fundamental understanding of the sensor processing-structure-property relationships. To this regard, we have developed a series of techniques [34, 35, 36, 37, 38] that enables the determination of the length and length distribution, diameter, molecular mass, mass density, defect density of SWCNTs in the dispersion. With assistance of these methods, the particular interesting and important questions to be answered regarding the processing-structure-property relationship of SWCNT-FibSen sensors are: how do the structures of SWCNTs in the dispersion affect the piezoresistive behavior of SWCNT-FibSen? What are the roles of SWCNT orientation/alignment states in dictating the piezoresistive mechanism(s) of CNT-based strain sensors? The answers to these questions are critical for optimizing the piezoresistive performance of SWCNT thin films and ultimately it may lead to producing highly sensitive SWCNT-FibSen sensors. Additionally, the fundamental knowledge acquired here can be valuable to help resolving a few apparently contradictory findings/conclusions derived from the simulation studies on the piezoresistive properties of CNT based strain sensors [39, 40, 41, 42, 43].

3. Methods and Procedures

3.1 Preparation of SWCNT dispersions

Purified single-wall carbon nanotube raw materials (HiPco® SWCNT) were purchased from Carbon Nanotechnologies Inc. (PO # 355) and used as-received. The SWCNT aqueous dispersion was prepared by sonicating a mixture of SWCNT, deionized water, and sodium dodecylbenzenesulfonate (SDBS, CAS # 25155-30-10, Sigma-Aldrich) in an ice bath using a Misonix 3000 probe sonicator (20 kHz). The sonicator was operated in a pulse operation mode (on 10 s, off 30 s) with the power set at 45 W. While maintaining a fixed SWCNT dispersion composition - 16 mg SWCNTs in 100 mL H₂O with 0.7 wt. % SDBS, we varied the effective sonication time (0.5 hr, 1 hr, 2 hr, 4 hr, 10 hr, 30 hr and 50 hr) to tailor the SWCNT length and bundle diameter in the dispersion. High-concentration dispersions were also similarly prepared by sonicating a mixture of 0.12 g SWCNT raw materials (Lot # PO258, Unidym™) and 2.4 g SDBS in 100 g deionized water in an ice bath using a Misonix 3000 probe sonicator (20 kHz). In some cases, mild sonication was performed by a Bransonic 2510 bath sonicator operated at 37 kHz in continuous mode with power level set at 100 W to minimize the cutting effect induced tube length shortening.

To further manipulate the structures of SWCNTs in the dispersion used for thin film preparation, the as-sonicated SWCNT dispersions were further subjected to an ultracentrifugation process for 2-hrs using Optima™ MAX-XP benchtop ultracentrifuge (Beckman Coulter, MLS-50 swinging bucket rotor) at a constant g-force acceleration. At the end of centrifugation process, the supernatant was carefully decanted and collected. With a similar protocol, the individualized SWCNT dispersions, in which the tubes are enriched with individual SWCNTs, were prepared by centrifuging an as-sonicated dispersion at 200,000 g-force for 2.45 hrs.

3.2 Characterization of SWCNT dispersions

3.2.1 Spectroscopic Characterization of SWCNT dispersions

A Renishaw inVia Raman microscope (785 nm excitation laser in backscattering geometry) was used for simultaneously collecting the Raman scattering and photoluminescence (PL) spectra of SWCNT dispersions. The simultaneously acquired Raman scattering and PL spectra allow the examination of the exfoliation or bundling states of SWCNT dispersion [44]. Attal et al. [45] demonstrated the use of UV-Visible absorption spectroscopy as a simple, accurate, convenient, and rapid tool for determining the SWCNT concentration in different surfactant-dispersed aqueous systems. By following a similar approach, we measured the optical absorbance – Abs of the SWCNT dispersion with a Varian Cary 5000 UV–Vis–NIR spectrometer (optical path $l = 0.5$ cm), which was then used for accurately determining the SWCNT concentration – C according to Beer's law: $\text{Abs} = \epsilon Cl$. In this practice, the previously determined ϵ value [44] $1.03 \pm 0.15 \times 10^{-18} \text{ cm}^2/\text{C-atom} = 0.052 \pm 0.008 \text{ L}/(\text{mg cm})$ was taken as the absorption cross-section of SWCNTs at 785 nm.

3.2.2 Sedimentation, Diffusion and Intrinsic Viscosity Measurement of SWCNT dispersions

With the Optima™ MAX-XP ultracentrifuge (Beckman Coulter, Inc., TLA-100.3, 30° fixed angle rotor) and a Varian Cary 5000 UV-Vis-NIR spectrometer, the PUM method developed previously [34] was applied to obtain the sedimentation functions of SWCNT dispersions (13,000 g-force for as-sonicated dispersions and 65,000 g-force for individualized dispersion). According to the analytical sedimentation solution derived by Mason et al. [46] and Shiragami et al. [47], the experimentally acquired sedimentation function was then numerically fitted to extract the bulk averaged sedimentation coefficient- s of SWCNTs.

Dynamic light scattering (DLS) was conducted by using a Delsa Nano C Particle Size Analyzer (Beckman Coulter, Inc.) to determine the diffusion coefficient D_G of SWCNTs in the dispersion. In DLS measurements, the time fluctuation of the scattered light intensity, $I_s(t)$, of the SWCNT dispersion was recorded at 25 °C at a fixed scattering angle of 165°. It was used for calculating the time correlation functions, $g_1(\tau)$, of the scattered electric field, which was then fitted by the well-known CONTIN method to extract the particle diffusion coefficient D_G .

An Ubbelohde capillary viscometer (Cannon Instrument Company, # 1B, calibration constant of 0.05) was used for measuring the viscosity of SWCNT dispersions at 25 °C with temperature controlled by an electro-thermostatic water cabinet (± 0.3 °C specified accuracy). During the measurement, the sample flow was videoed at 25 frames per second, which was then image processed for accurately determining the flow time. As an error control protocol, the viscosity of pure water ($\rho = 0.998 \text{ g/cm}^3$ at 25 °C) was measured at the end of each sample

test and compared with the standard value. With this practice, a total of 31 measurements on water were performed during the entire course of SWCNT dispersion viscosity test. It resulted in an averaged viscosity of 0.899 ± 0.007 cP. This value is slightly higher than the standard viscosity 0.8902 cP of water at 25 °C [48]. This difference is attributed to the kinetic energy effect caused by the relatively short flow time of water (17.99 ± 0.15 sec) in capillary # 1B. With the standard value of 0.8902 cP as a calibration, the kinetic energy corrected Poiseuille relation for the # 1B capillary was obtained as η (cP) = $0.05t - 0.168/t$. This relation was further used to calculate the viscosity of a given SWCNT dispersion and its diluted samples according to the experimentally measured flow time. Typically, each of the as-prepared SWCNT dispersion of concentration C_0 was diluted to 4 - 5 samples with concentration ranging from $(0.2 - 1) \times C_0$ for viscosity test. The corresponding SWCNT concentration (g/cm³) was determined by UV-Vis-NIR spectroscopy according to the procedures described previously. According to Eq. (1) (See Results and Discussion), a linear fitting of the SWCNT concentration against the corresponding dispersion viscosity was applied to determine the intrinsic viscosity $[\eta]_c$.

3.2.3 Microscopy examination of SWCNT dispersions

High-resolution transmission electron microscopy (HR-TEM, JEM-ARM200cF, JEOL Ltd.) was applied for qualitative examination of the morphologies of SWCNTs. The TEM sample was prepared by drop casting and drying SWCNT dispersion on a Lacey grid (300 mesh Cu: Ted Pella). The tapping mode AFM (Veeco Instruments, Inc. Multimode) was used to acquire images of the individualized SWCNTs on a silicon wafer substrate under ambient conditions to determine the length distribution and validate the GEP-SRSPL results. The experimental details for GEP-SRSPL method is given below.

3.2.4 Gel Electrophoresis of SWCNTs mapped by Simultaneous Raman scattering and Photoluminescence spectroscopy

Agarose gel with fixed solid content of 0.7 wt. % was prepared for performing the gel electrophoresis of SWCNT dispersion. In brief, 1.05 grams of agarose powder (BE A500, LOT# - 12D2005, MIDSCI – Laboratory Equipment & Supplies) was dissolved in 150 ml of 0.7 wt. % SDBS aqueous solution by magnetic stirring at elevated temperature. The clear agarose solution was subsequently cooled to 55°C and then poured into a gel casting tray (15 cm × 10 cm) for further cooling and gel formation. During this process, a comb template was inserted for forming sample loading well. To perform the gel electrophoresis of SWCNT dispersion, the fully gelled agarose slab was carefully placed into the electrophoresis chamber (17.5 cm × 26.5 cm gel tank, E1015-10-GT - VMR® Midi plus Horizontal Electrophoresis system), in which 400ml of 0.7 wt. % SDBS aqueous solution was filled as the buffer solution. In a typical electrophoresis run, the individualized SWCNT dispersion was loaded and subjected to a constant electric field of 10V/26 cm = 0.385 V/cm for 1 hr. Varied field strength was also examined to verify that, with this field strength setting, the electrophoresis mobility of SWCNTs is field-independent. Immediately after the electrophoresis, the gel sample was then cut into a small block (2.5cm × 1.5cm × 1.0cm) for mapping the Raman scattering spectra of electrophoresed SWCNTs with a Reinshaw inVia Raman microscope. The Raman mapping process was facilitated by a computer-controlled motorized XYZ sample stage that has a step resolution of 1 μm. The gel block, which was supported by a glass slide and mounted on the XYZ stage, was mapped along the electrophoresis trace with the sample well as the origin and equal spaced interval (200 μm per

spectrum) for simultaneous collection of the Raman scattering and PL emission spectra of electrophoresed SWCNTs. The spectra were collected in backscattering geometry by a 5× objective with a 785 nm (1.58 eV) diode laser as the excitation source. The beam size was approximately 100 μm \times 150 μm . For each mapping process, a small-sized silicon wafer was positioned beside the sample well as a reference for facilitating laser beam focus. No attempt was taken to re-adjust the focus during the mapping process. This is critical for eliminating the optics change induced intensity variation so that one can directly associate the detected Raman and PL intensity to the SWCNT concentration. The experimental procedure for SRSPL mapping was validated by mapping the Raman spectra of a silicon wafer placed on a cut gel block. Over the entire mapping range, the relative variation of the Raman intensity of the silicon wafer was found to be 1.8 %, which confirms the mapping protocols described above.

3.3 Fabrication of SWCNT thin film piezoresistive sensors

Spray coating was carried out with Iwata Eclipse HP-BS airbrush operated at 200 kPa to deposit an appropriate amount of SWCNT dispersion on a substrate for fabricating SWCNT thin films. Two different types of substrates were selected. One was biaxially stretched polyethylene terephthalate (PET) film 0.25 mm thick (ES301450, Goodfellow Corp.). The other was a polydimethylsiloxane (PDMS) sheet prepared in-house by mold casting of Sylgard 184 silicone elastomer kit purchased from Dow Corning. The formulation and curing conditions provided by the vendor were followed in preparing PDMS substrate. Namely, 10 parts base silicone polymer was thoroughly mixed with 1 part curing agent. The mixture was then cast into a glass mold and cured at 100°C for 2 hrs. The sensors supported by a PET substrate and PDMS substrate, which are respectively termed as PET and PDMS sensors, were used for studying the SWCNT thin film sensing characteristics for small-deformation (< 2 % tensile strain) and large deformation (up to 30 % tensile strain), respectively. The strain-to-failure for PET and PDMS substrate were 3 % and 60 % respectively.

In the spray process, the substrate was heated by a hot plate (1000-1 Precision Hot Plate, Electronic Micro Systems Ltd.) set at 85°C to accelerate the solvent (water) evaporation and facilitate thin film formation. In addition, the spray was confined to a predetermined region such that the SWCNT thin film formed on the substrate had a rectangular shape. Typically, the size of SWCNT thin film formed on PET substrate was 3.5 cm \times 3.5 cm, and was 1 cm \times 1.5 cm on the PDMS substrate. After the spraying process, the as-prepared SWCNT thin film was further subjected to immersion treatment in deionized H₂O overnight to remove the residual SDBS molecules. Followed by an immersion treatment, the SWCNT thin film was dried in air at ambient temperature and ready for the subsequent attachment of electrodes in preparing the piezoresistive sensors. Both 4-probe and 2-probe configurations were attempted in electrode preparation. In the 4-probe configuration, four copper wires were fixed to the corners of the rectangular SWCNT thin film by using silver paste. In the 2-probe configuration, the self-adhesive conductive copper tape was applied to the two end-sides of the rectangular SWCNT thin film for electrode preparation. After attaching the electrodes, the PDMS sensor was further packaged in PDMS matrix by following the similar procedure that was described previously for PDMS substrate preparation. The packaging process prevents the electrode from detaching when the sensor is subjected to coupled electrical-mechanical test in large deformation tests.

The packaging process was not applied to PET sensor, since its sensing characteristics was mainly studied for small deformation tests.

To prepare the mechanically-drawn SWCNT thin films, the undrawn film on PET substrate cut into a strip of width $W_0 = 0.4$ cm was stretched by a Q800 dynamic mechanical analyzer (DMA, TA instruments) with the gauge length set at $L_0 = 0.8$ cm. The strip to be stretched was first equilibrated at 220°C for 10 mins and then isothermally drawn to the specified final length L at a strain rate of 1%/min. While the stretched strip was maintained at the final length, the furnace was cooled down to room temperature to finally give the mechanically-drawn SWCNT thin film with the desired draw ratio ($\lambda = L/L_0$). With this procedure, a series of SWCNT thin films with draw ratio of $\lambda = 1.2, 1.5, 2.0, 2.2, 2.5, 2.75$ and 3.2 were prepared.

3.4 Continuous fabrication of SWCNT-FibSen sensors

Different types of fibers in single filament form, which include glass fiber (woven roving, part # 223, 20 μm in diameter, Fibre Glast Developments Corp.), polyaramid fiber (Twaron[®] 2200, AR305768, 12 μm in diameter, Goodfellow Corp.), Nylon fiber (25 μm in diameter, Invista Inc.), and PET fiber (ES305720, 17 μm in diameter, Goodfellow Corp.), were used as the substrate for fabricating SWCNT thin film coated SWCNT-FibSen fiber sensors. The SWCNT-FibSen sensor was fabricated by an in-house developed continuous spray coating system, which is schematically shown in Figure 1. The key elements for this system is composed of a computer controlled stepper motor (Silverpak 17C with PW-100-24 power supply, Lin Engineering Corps.) and a series of pulley modules for conveying the fiber filament through a spray coating station, heating station, and immersion washing station. In a typical coating process, the motor winding speed was set at ~ 1 cm/min. The spray coating station is assembled by fixing a spraying nozzle (adjustable nozzle set, part # AD-NOZ_001, Nanotrons Corp.) on a steel rod to distribute SWCNT dispersion mist on to the fiber filament. An Iwata air compressor operated at 200 kPa was used to deliver SWCNT dispersion to the nozzle. Downstream of the spray coating station is a heating station, which is composed of a heat gun (Master Heat Gun[®], HG-301A, 260°C) set 20 cm away from the fiber filament for evaporating water to accelerate the SWCNT thin film formation. After the heating station, the SWCNT thin film coated fiber filament was then passed through a bath of deionized water to remove the residual SDBS molecules. After the immersion washing process, the SWCNT-FibSen sensor was then dried in air at ambient temperature and ready for later use.

3.5 Fabrication of glass fiber reinforced composite (GFRC) laminates embedded with SWCNT-FibSen sensors

A vacuum bagging process was used to fabricate fiberglass preregs (Prepreg 7781 E-Glass, part # 3100, 27 % to 33 % resin content, 0/90 fiber orientation, Fibre Glast Developments Corp.) into laminate coupon samples to demonstrate the use of SWCNT-FibSen sensors for monitoring the resin curing during the composite manufacturing process, mapping the stress/strain field and detecting damage and failure for SHM of composite structures. A typical laminate coupon was composed of 2-layer (for cyclic tension and compression as well as tension-to-failure test) or 3-layer (for cyclic 3-point bending test) stacked preregs, which were pre-cut into a rectangular shape of ~ 5 cm \times ~ 2 cm before use. With the pre-determined

orientation and position design, a single or multiple SWCNT- FibSen sensors and the corresponding gold wire electrodes ($\sim 50 \mu\text{m}$ diameter, LOT # 29001, California Fine Wire Company) were manually sandwiched between the prepreg stacks. The prepreps embedded with SWCNT-FibSen sensors were then placed in a vacuum bag system that was operated at one standard atmospheric pressure (0.1 MPa) and heated by a hot plate (Manual Hydraulic Press, Specac Corp.) to induce the resin curing process. The curing protocols suggested by the prepreg vendor were followed: temperature first ramped from room temperature to 143°C and then maintained at 143°C isothermally for 2 hrs. In the prepreg curing process, the resistance change of the embedded SWCNT-FibSen sensor was simultaneously monitored by a Keithley 2401 Sourcemeter[®] controlled by a homemade LabVIEW user interface.

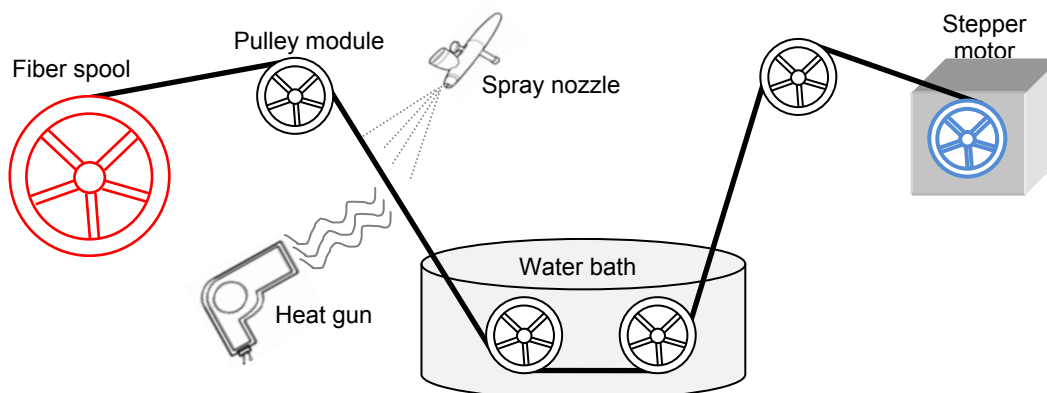


Figure 1. A schematic diagram of the continuous spray coating process for fabricating SWCNT-FibSen sensor.

3.6 Characterization and Piezoresistivity Evaluation of Various SWCNT sensors

Scanning electron microscopy (SEM) was performed with JEOL 7400 at 10 kV for examining the morphologies of SWCNT thin films, both oriented and unoriented. The samples were sputter coated with gold prior to SEM imaging. The same instrument was also used to acquire the EDX (Energy dispersive X-ray) spectra to examine the residual SDBS molecules in the SWCNT thin film samples. A Varian Cary 5000 UV-vis-NIR spectrometer was used to record the optical absorption spectra of SWCNT thin film piezoresistive sensors from 300 nm to 1300 nm. In the measurements, blank PET and PDMS substrates were used as the reference respectively for the PET sensors and PDMS sensors.

Coupled electrical-mechanical testing was applied to evaluate the sensing characteristics of SWCNT thin film piezoresistive sensors. The PET or PDMS sensor was subjected to cyclic tensile deformation applied by AGS-J mechanical test machine (Shimadzu Scientific Instruments, Inc., 500 N load cell). The typical settings in the tensile test of PET sensors were: 10 mm gauge length, 0.2 mm maximum displacement, and 0.5 mm/min displacement rate. The cyclic tensile test settings for PDMS sensors were: 10.5 mm gauge length, 3 mm maximum displacement, and 2 mm/min displacement rate. While the SWCNT thin film piezoresistive sensors were subjected to cyclic tensile deformation, the electrical resistance of the sensor was simultaneously measured. The real-time resistance for the sensor with 2-probe electrode

configuration was recorded by a Keithley 2182A nanovoltmeter and Keithley 6221 current source controlled by a homemade LabVIEW user interface. The resistance change for the sensors with 4-probe electrode configuration was examined according to the van der Pauw method [49] by using the same setup in conjunction with an Agilent 3499B switch/control system. Due to the limitation of the switching speed of Agilent 3499B, measuring the real-time resistance change in 4-probe configuration was not feasible. Instead, the resistance for the sensors with 4-probe electrode configuration was measured statically at a set of discrete strain levels.

The piezoresistivity of the standalone SWCNT-FibSen sensor was tested at room temperature by a coupled electrical-cyclic tensile testing method. The fiber sensor, glued on a perforated cardboard and applied with silver paste on its two ends as electrodes, was subjected to cyclic mechanical tension at room temperature applied by a dynamic mechanical analyzer (Q800, TA Instrument Inc.). For DMA measurement, the gauge length, the amplitude of the displacement and displacement rate were respectively set at 8.5 mm, 0.1 mm and 0.4 mm/min. An AGS-J mechanical test machine (500 N load cell, Shimadzu Scientific Instruments, Inc.) was used to apply varied mechanical deformation mode – cyclic tension, cyclic compression, cyclic 3-point bending, and tension-to-failure test to the laminates in which the SWCNT-FibSen sensors were embedded. The typical conditions for AGS-J tests were: for cyclic tension, the gauge length, the amplitude of the displacement, and the displacement rate were respectively set at 20 mm, 0.2 mm and 1 mm/min; for cyclic compression, the amplitude of the displacement and displacement rate were respectively set at 0.4 mm and 3 mm/min; for cyclic 3-point bending, the maximum span, the amplitude of the displacement and displacement rate were respectively set at 30 mm, 4 mm and 20 mm/min; and for tension to failure test, the gauge length of the specimen was set at 20 mm and stretched to failure at a displacement rate of 1 mm/min. During DMA and AGS-J test, a Keithley 2401 Sourcemeter® controlled by a homemade LabVIEW user interface was used for recording the sensor resistance. The same electronic devices in combination with an Agilent 3499B switch/control system and a 44473A 4×4 matrix module (Max. scan rate ~ 0.02 second/channel) were used for simultaneously recording the resistance when multiple sensors were involved.

Polarized Raman spectroscopy was applied to quantitatively determine the degree of orientation of the mechanically-drawn SWCNT thin films. In brief, the polarized Raman spectra of the stretched SWCNT thin films were collected at room temperature by a Reinshaw inVia Raman microscope in a backscattering configuration using a 785 nm excitation laser with the nominal power set to 30 mW. A 5× objective was used to focus the laser beam to result in a beam size of approximately 100 μm × 150 μm. A computer-controlled rotational stage was used to rotate the film sample around the laser beam to vary the angle Φ , which was formed between the polarization direction of the incident laser beam and the drawing direction of the SWCNT thin film, from 0° to 180° at an interval of 15°. At each Φ , both VV and VH Raman spectra were acquired in the range of 100 cm⁻¹ to 3200 cm⁻¹. In VV configuration, the polarization of the incident laser beam is parallel to that of the scattered beam; and in VH configuration, the polarization of the incident laser beam is perpendicular to that of the scattered beam. According to the procedures given in [50], one can then extract the orientation

order parameter of SWCNTs by using the Raman intensity variations for both VV and VH spectra with respect to the azimuthal angle Φ .

4. Results and Discussion

4.1 Structural characterizations of SWCNT dispersion

4.1.1 Combined intrinsic viscosity, sedimentation and diffusion measurements for determining the length, diameter, molecular mass, mass density and surfactant adsorption

When polymers or colloidal particles are dissolved or dispersed in a solvent, the viscosity of the solution/dispersion (η) relative to that of the neat solvent (η_0) is increased. At very low polymer/particle concentration (C) or volume fraction (ϕ), the viscosity of the solution/dispersion is given by [51,52]:

$$\eta \approx \eta_0 (1 + [\eta]_c C) = \eta_0 (1 + [\eta]_\phi \phi) \quad \text{Eq. (1)}$$

where the coefficient $[\eta]_c$ or $[\eta]_\phi$ is the intrinsic viscosity - a measure of the hydrodynamic volume of the dissolved polymer or dispersed particle. $[\eta]_c$ (cm³/g) is related to $[\eta]_\phi$ (dimensionless) through the density ρ of the polymer/particle by:

$$[\eta]_\phi = \rho [\eta]_c \quad \text{Eq. (2)}$$

By considering the analogy between electrostatics and hydrodynamics, Mansfield and Douglas accurately computed the intrinsic viscosity of the rodlike particles by path integral approach [53]. According to their calculations, the dimensionless intrinsic viscosity for a cylindrical particle of length L and diameter d is given by:

$$[\eta]_\phi = \frac{8A^2}{45} \left[\ln \left(\frac{4A}{e^{12}} \right) \right]^{-1} \times \left[\frac{1 - 1.178t + 1.233t^{1.86} + 1.925t^{6.28} + 0.625t^{12.67}}{1 - 1.094t + 0.757t^{3.76} + 1.344t^{3.83} + 1.978t^{12.07}} \right] \quad \text{Eq. (3)}$$

where $A = L/d$ is the aspect ratio of the rod; and $t = 1/\ln(A)$. As indicated by Eq. (2) and Eq. (3), if the particle density is known, the aspect ratio A for a rodlike particle can be determined by measuring the intrinsic viscosity $[\eta]_c$. With a further assumption of the rod diameter d , the rod length L can be accordingly calculated from A . This is exactly the approach taken by Parra-Vasquez et al. for measuring the length of individualized SWCNTs [54]. However, this approach does not apply to SWCNT bundles – a typical product of as-sonicated SWCNT dispersion. First, the bundle diameter is not a constant and it decreases with the exfoliation process. Second, the density of SWCNT bundles is not known a priori and it may vary with the adsorption of surfactant molecules. This difficulty, as shown below, can be overcome by a combined measurement of intrinsic viscosity, sedimentation coefficient and diffusion coefficient of SWCNT dispersions.

According to the hydrodynamic calculations by Tirado [55] and Broersam [56] the translational friction coefficient, ζ_t , for a rodlike particle is given by:

$$\begin{aligned} \zeta_t &= 1500\pi\eta_0 LQ(A) \\ &= 1500\pi\eta_0 L \left\{ \frac{(\ln 2A)^4}{[500 \ln(A) + 188](\ln 2A)^4 - 75(\ln 2A)^3 - 5400(\ln 2A)^2 + 13750 \ln(2A) - 7750} \right\} \end{aligned} \quad \text{Eq. (4)}$$

By using Eq. (4) and the definition of sedimentation coefficient – s:

$$s = \frac{m(1 - \rho_0 / \rho)}{\zeta_t} = \frac{\nu(\rho - \rho_0)}{\zeta_t} = \frac{\pi d^2 L (\rho - \rho_0)}{4 \zeta_t} \quad \text{Eq. (5)}$$

and the mass-of-center diffusion coefficient – D_G :

$$D_G = \frac{k_B T}{\zeta_t} \quad \text{Eq. (6)}$$

we can establish the relationship between the experimentally measured quantity s and D_G with respect to $[\eta]_c$ as:

$$s D_G^2 = \left(\frac{k_B T}{2 \pi A} \right)^2 \left(\frac{1}{1500 \eta_0 Q(A)} \right)^3 \left[\frac{[\eta]_\phi(A)}{[\eta]_c} - \rho_0 \right] \quad \text{Eq. (7)}$$

In Eq. (7), ρ_0 and η_0 are respectively the solvent density and viscosity measured at temperature T; k_B is the Boltzmann constant. The expressions for $Q(A)$ and $[\eta]_\phi(A)$ can be found in Eq. (4) and Eq. (3), respectively. With the help of Eq. (7), a combined measurement of $[\eta]_c$, s, and D_G can be used for uniquely determining the rod aspect ratio – A, from which the rod density – ρ , volume – ν , mass – m, length – L and diameter – d can also be derived accordingly. The results are gives as following:

$$\rho = \frac{[\eta]_\phi(A)}{[\eta]_c} \quad \text{Eq. (8a)}$$

$$\nu = \frac{s}{D_G} \frac{k_B T}{\rho - \rho_0} \quad \text{Eq. (8b)}$$

$$m = \rho \nu \quad \text{Eq. (8c)}$$

$$d = \left[\frac{4 \nu}{\pi A} \right]^{1/3} \quad \text{Eq. (8d)}$$

$$L = A d \quad \text{Eq. (8e)}$$

As an alternative to Eq. (4), the friction coefficient for rigid rods based on an asymptotic hydrodynamic model [57] was also used to determine L and d by:

$$s = \frac{(\rho_0 - \rho) d^2}{12 \eta} \left[\ln \left(\frac{L}{d} \right) + 2 \ln 2 - 1 \right] \quad \text{Eq. (9)}$$

$$D_G = \frac{k_B T}{3 \pi \eta L} \left[\ln \left(\frac{L}{d} \right) + 2 \ln 2 - 1 \right] \quad \text{Eq. (10)}$$

where ρ and ρ_0 are respectively the density of the dispersed particle and the solvent, η is the viscosity of the solvent. To use the simplified Eq. (9) and (10), one has to assume the density of SWCNTs in the dispersion to determine the length and diameter.

With the experimentally determined results of s , D_G , and $[\eta]_c$, the length L , diameter d , aspect ratio A , density ρ , and molecular mass M of the SWCNTs in different dispersions can be accordingly calculated by Eq. (7) and Eq. (8). Figure 2a shows such determined length and diameter values for the SWCNTs sonicated at varied conditions. It clearly shows a power-law relationship between d and L - $d = 0.12L^{0.62}$ - a consequence of simultaneous cutting and exfoliation of SWCNT bundles. The rigid rod behavior of SWCNTs can be recovered by considering the relationship between the dimensionless intrinsic viscosity $[\eta]_\phi$ and the aspect ratio $A = L/d$. Figure 2b shows the plot of $[\eta]_\phi$ against $A = L/d$. In the same figure, we also include the results of individualized SWCNTs reported in [54] for comparison. As can be seen from Figure 2b, all the SWCNT samples - the as-sonicated bundles and the individual tubes from different work obey the theoretically predicted power-law relationship for rigid rods - $[\eta]_\phi \propto (L/d)^{1.76}$.

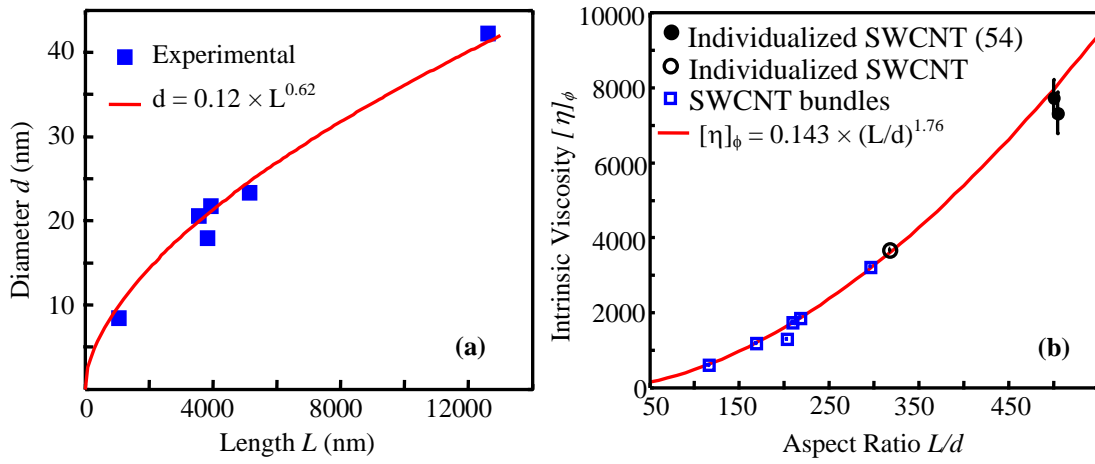


Figure 2. Power-law relationship between (a) SWCNT bundle length L and diameter d , (b) the dimensionless intrinsic viscosity $[\eta]_\phi$ and the rod aspect ratio (L/d) for SWCNT bundles and individualized tubes prepared at different conditions.

Previous studies [58, 59, 60] suggested that the surface coverage of SDBS - n_{SDBS} strongly depends upon the curvature of the substrate being adsorbed. For an individual tube, n_{SDBS} can be as high as $22.5 \text{ molecules/nm}^2$; and for a flat graphite surface, a very low value of $n_{\text{SDBS}} = 1.45 \text{ molecules/nm}^2$ was observed. These early findings suggest the curvature effect of SDBS adsorption on SWCNT bundles. Namely, the value of n_{SDBS} expects to decrease with increasing the SWCNT bundle diameter. To examine this speculation, we calculated the values of n_{SDBS} for all the SWCNT bundle samples. In the calculation, the density ρ_b of a pristine SWCNT bundle and the SDBS adsorption thickness l_c were respectively taken as 1.55 g/cm^3 and 2.51 nm . The results are shown in Figure 3. Within the experimental error, the curvature effect of SDBS adsorption on SWCNTs is clearly born out. Specifically, the larger is the SWCNT bundle diameter, the smaller is the SDBS surface coverage.

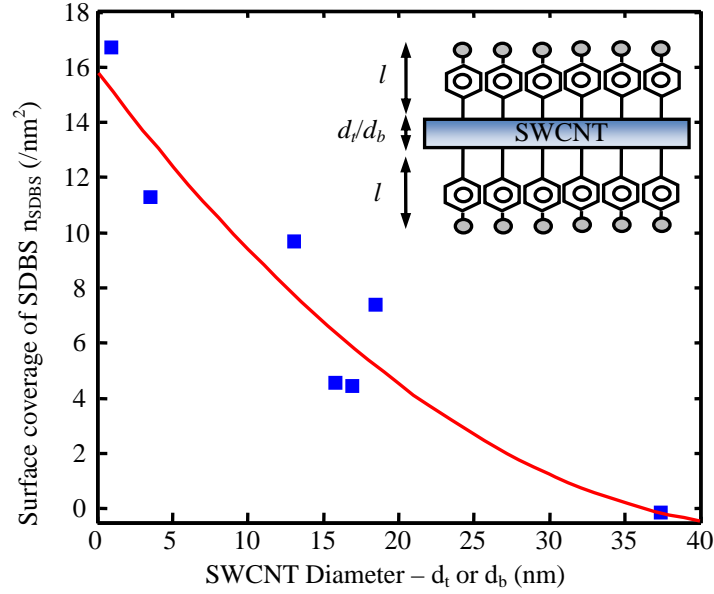


Figure 3. Effect of SWCNT diameter - d_t or d_b on the surface coverage of SDBS adsorption. Solid line is a guide to the eye. Inset is the adsorption model to depict a monolayer of SDBS adsorbed on SWCNT with thickness $l_c = 2.51$ nm.

4.2.2 Gel Electrophoresis and Raman Mapping for Determining the Length Distribution of SWCNTs

GEP has been proved to be a viable technique to sort SWCNTs by lengths [61]. Under the influence of an applied electric field, the SWCNTs of longer length have difficulty traveling through the gel and show small mobility; while the SWCNTs of shorter lengths migrate through the gel faster and have large mobility. The electrophoretic mobility μ is defined as the migration speed V_m under unit electric field strength. With this definition, the SWCNT length-dependent mobility, μ , measured along the electrophoresis trace from the edge of the loading well at distance S is given by:

$$\mu(L) = \frac{V_m}{E} = \frac{S}{Et} \quad \text{Eq. (11)}$$

where t is the time duration of the electrophoresis process and the typical setting in our experiments is 1 hr.; and E is a constant field strength. The inset of Figure 4 shows a photograph of the electrophoresis trace of the S2hr-200kg dispersion – an individualized SWCNT dispersion prepared by centrifuging a two-hour sonicated SWCNT dispersion at 200,000 g-force for 2.45 hrs. The broad dark band observed suggests the sample S2hr-200kg has a broad SWCNT length distribution. In the electrophoresis direction indicated by the dashed-line arrow, the SWCNTs with shorter length/higher mobility are located in the front of the band and the SWCNTs with longer length/smaller mobility are present in the rear of the band. The mobility distribution $f(\mu)$ of SWCNTs can be obtained by mapping the SWCNT concentration along the electrophoresis trace. This was performed by using the simultaneous Raman scattering and photoluminescence (SRSPL) spectroscopy as detailed in the experimental section and the results are shown in Figure 5.

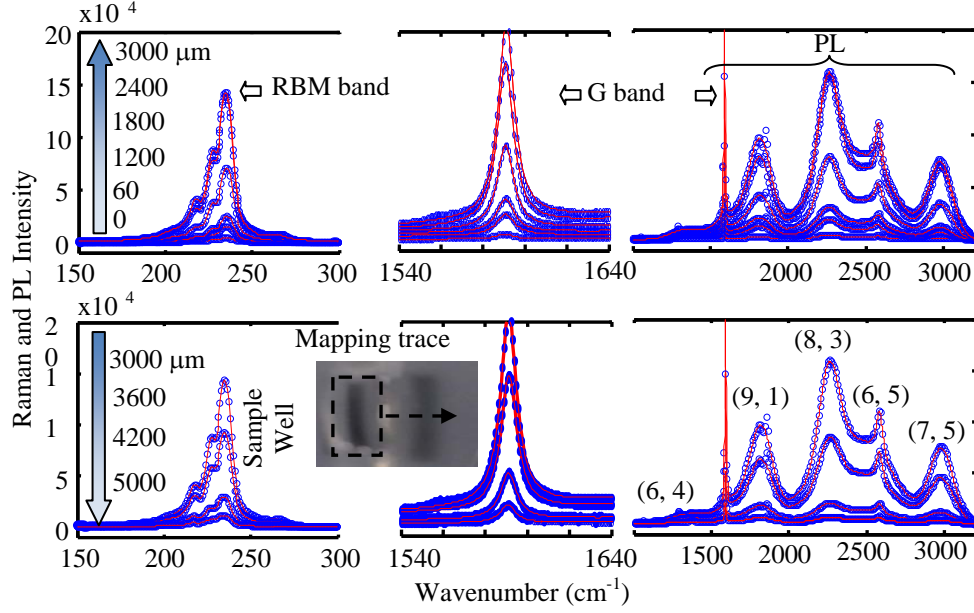


Figure 4. SRSPL spectra of S2hr-200kg mapped along the electrophoresis trace at different distances. The PL emission band of (6, 5) tube is superposed with the Raman G' band (2577 cm⁻¹). The inset is the photograph of the individualized SWCNTs (S2hr-200kg) experienced gel electrophoresis in agarose for 1hr at an electric field of 0.385 V/cm.

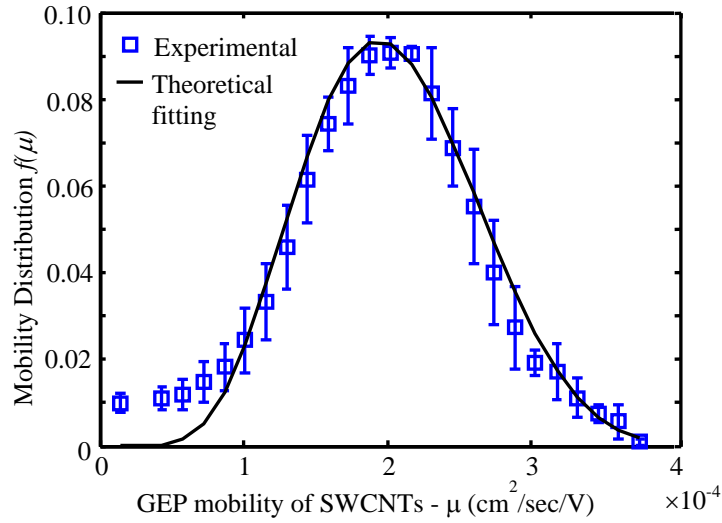


Figure 5. The SWCNT mobility distribution $f(\mu)$ for S2hr-200kg derived from the GEP-SRSPL mapping. The scattered data are the experimental results. The smooth curve is a theoretically fitted result by considering Eq. (12) and the lognormal distribution - $g(L)$ of the SWCNT length determined by AFM measurements. The fitting parameters are $A = 1985.3$ and $B = 10.2$.

To derive the length distribution $g(L)$ from $f(\mu)$, a functional relationship between μ and L for the SWCNTs is necessary. A simple empirical function

$$\frac{1}{\mu(L)} = A + BL \quad \text{Eq. (12)}$$

is attempted for this purpose. In Eq. (12), the coefficients A and B take into account the effect of charge density of SWCNTs, gel composition and structures, and SWCNT/gel interactions. The μ - L relation in Eq. (12) has been successfully used to describe the length dependent GEP mobility for a variety of biopolymers, such as DNAs with a broad range of length [62,63,64] as well as the rod-like bacteriophage fd (length varied from 367 nm to 2808 nm) [65]. The appropriateness of Eq. (12) in describing the μ - L relation of SWCNTs can be further examined by comparing the $f(\mu)$ of S2hr-200kg determined by GEP-SRSPL with the one derived from its length distribution $g(L)$ as measured by AFM (Figure 6). With the lognormal distribution (mean value of 489.5 nm and standard deviation of 290.5 nm) determined by AFM for S2hr-200kg, we can accordingly derive its mobility distribution $f(\mu)$ by using Eq. (12). By setting the parameters $A = 1985.3$ and $B = 10.2$, the best fitted $f(\mu)$ for S2hr-200kg derived from the AFM length distribution was obtained and the result is shown in Figure 5. Clearly, except for the small portion of the distribution at low mobility end, the $f(\mu)$ derived from the AFM measurement agrees reasonably well with that directly measured by GEP-SRSPL. This agreement confirms Eq. (12) as a useful and reasonable tool in describing the μ - L relationship for the GEP of SWCNTs. With this relation, the length distribution $g(L)$ can be derived from the GEP mobility distribution $f(\mu)$, if the values of A and B are known. As shown below, for a given SWCNT dispersion, the values of A and B can be determined by the new method - GEP-SRSPL developed in this project.

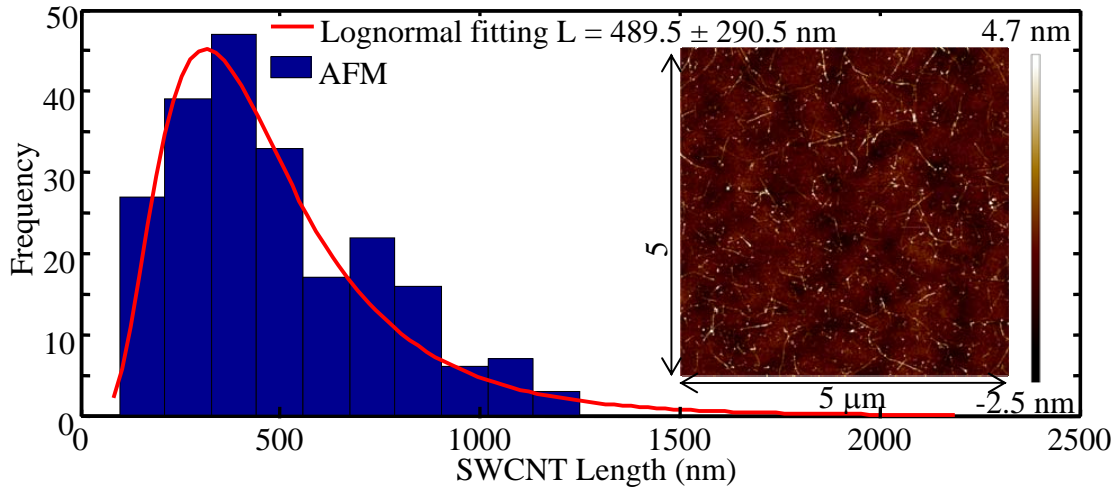


Figure 6. AFM results for the length distribution of the individualized SWCNT sample - S2hr-200kg.

It has been well established that the PL quantum yield of SWCNT - ϕ strongly depends on the tube length and its internal defect density [66, 67, 68]. A closed-form solution of ϕ for a defective SWCNT of finite length L has been developed in our previous work [35], which is given by Eq. (13):

$$\phi = \phi(\infty, 0) \left\{ 1 - 2\nu_n \left[\ln \frac{\nu_n}{2} + 2 \ln \frac{\Gamma(\frac{\nu_n}{2})}{\Gamma(\frac{\nu_n+1}{2})} \right] \right\}, \quad \nu_n = l_\infty \left(m + \frac{1}{L} \right) \quad \text{Eq. (13)}$$

where $\phi(\infty, 0)$ represents the intrinsic PL quantum yield of a SWCNT with infinite length and zero defect density; ν_n is a parameter to characterize the defect density, in which l_∞ is the exciton diffusion length, m is the number density of the internal defects associated with a given SWCNT, and $1/L$ accounts for one defect formed by the two ends the SWCNT of finite length. By linking with the SRSPL experiments and considering the μ - L relation in Eq. (12), Eq. (13) can be re-written as:

$$\frac{I_{PL}}{I_G} = P_1 \left\{ 1 - 2\nu_n \left[\ln \frac{\nu_n}{2} + 2 \ln \frac{\Gamma(\frac{\nu_n}{2})}{\Gamma(\frac{\nu_n+1}{2})} \right] \right\}, \quad \nu_n = P_2 + \frac{P_3\mu}{1 - P_4\mu} \quad \text{Eq. (14a)}$$

$$P_1 = \frac{\varepsilon\phi(\infty, 0)}{\beta}, \quad P_2 = l_\infty m, \quad P_3 = l_\infty B, \quad P_4 = A \quad \text{Eq. (14b)}$$

In Eq. (14), the newly appeared parameters that have not been defined previously are the intrinsic optical absorption cross section ε and Raman scattering cross section β of SWCNTs. IPL and IG are respectively the intensity of a PL band and a Raman band experimentally determined through GEP-SRSPL mapping. By fitting the experimentally measured data set of μ vs. I_{PL}/I_G , the four unknown parameters $P_1 - P_4$ can be determined, from which the coefficients A and B of the μ - L relation can be accordingly derived as $A = P_4$ and $B = P_3/l_\infty$. Eq. (14) was applied to fit μ vs. I_{PL-SUM}/I_G results of the S2hr-200kg sample acquired from the GEP-SRSPL spectra, where I_{PL-SUM} is the intensity summed over all the five PL bands as shown in Figure 4. With the peak-fitting procedures, one can also use the individually resolved PL bands to calculate $I_{PL-(n,m)}/I_G$ for a specific (n, m) tube. The advantage of using I_{PL-SUM} over $I_{PL-(n,m)}$ is to avoid the uncertainties/ambiguities involved in the peak fitting process. Figure 7a shows the experimentally determined μ vs. I_{PL-SUM}/I_G for S2hr-200kg averaged over three repeating GEP runs. As shown in Figure 7a, one notes an initial increasing trend of the I_{PL-SUM}/I_G with μ . This is a result of the presence of small amount of SWCNT bundles in the S2hr-200kg sample. Due to bundling, the PL emission of SWCNTs can be quenched to cause the reduced PL intensity and therefore the value of I_{PL-SUM}/I_G . With exclusion of the few data points at small values of μ , the μ vs. I_{PL-SUM}/I_G for s2hr-200kg was fitted according to Eq. (14) and the results are shown in Figure 7a. The coefficient A obtained by fitting the GEP-SRSPL spectra is 1875.1, which agrees very well with the value of $A = 1958.3$ determine by AFM measurements (Figure 5 and 6). Such agreement further confirms the validity of μ - L relationship as described by Eq. (12) and the usefulness of Eq. (14) in extracting the structural parameters of SWCNT by using the GEP-SRSPL technique. This point can be further strengthened by a good agreement between the length distribution of S2hr-200kg determined by AFM and the one calculated according to its mobility distribution through using the μ - L relationship with the coefficient $A = 1875.1$ and $B = 10.2$. The result is shown in Figure 7b.

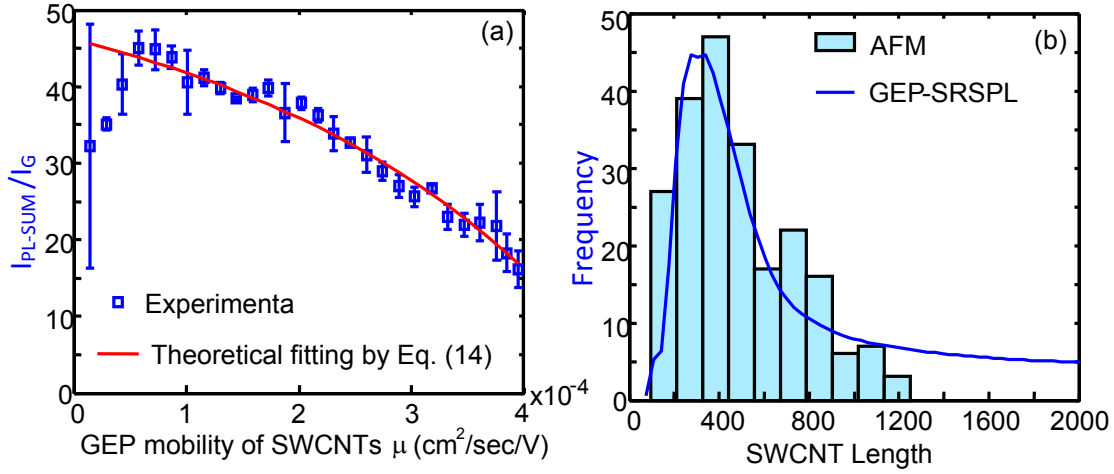


Figure 7. (a) Relationship between the GEP mobility and the G-band normalized PL intensity – $I_{\text{PL-SUM}}/I_{\text{G}}$ for S2hr-200kg sample: the experimental results versus theoretical fitting according to Eq. (11). The fitting parameters are: $P1 = 656.3$, $P2 = 1.254$, $P3 = 714.7$, and $P4 = 1875.1$ b) A comparison of the length distribution of S2hr-200kg measured by AFM and calculated according to its mobility distribution determined by GEP-SRSPL through using the μ - L relationship with the coefficient $A = 1875.1$ and $B = 10.2$.

4.2 Processing-Structure-Property Relationships of SWCNT thin film Piezoresistive Sensors

4.2.1 Effects of film thickness and SWCNT structures

To answer the question how the structures of SWCNTs in the dispersion affect the piezoresistive behavior of SWCNT thin film based piezoresistive sensors, we varied the sonication conditions to prepare the SWCNT aqueous dispersions that cover a broad range of SWCNT diameters and lengths. For all these dispersions, Table 1 provides the results of sedimentation coefficient - s , diffusion coefficient – D_{G} , and the bulk averaged length and diameter of SWCNT bundles calculated according to Eq. (9) and (10). The relative error (ratio of one standard deviation to the mean value) of the sedimentation coefficient was previously estimated to be $\sim 20\%$ [34]. With Monte Carlo simulation [69], the accordingly calculated SWCNT length and bundle diameter was determined to have a relative error of 6.7% and 12.4%, respectively. With these dispersions, the corresponding SWCNT thin films were prepared by spraying coating on both PDMS and PET substrate to investigate the effects of SWCNT structures on the piezoresistivity of SWCNT thin film sensors. Figure 8 shows the representative coupled electrical-cyclic tensile testing results for a PET sensor (Figure 8(a), 2hr-sonicated dispersion sprayed at 20 ml) and a PDMS sensor (Figure 8(b), 50hr-sonicated sprayed at 10 ml). In the cyclic tensile testing, the maximum tensile strain applied to the PET sensors and PDMS sensors were respectively set at $\sim 2\%$ and $\sim 30\%$. As shown in Figure 8(a), the PET sensor showed very good linearity on the piezoresistive response in the range of the applied tensile strain (0 – 2 %). The gauge factor GF, which is a measure of the sensor sensitivity, was evaluated for the PET sensors by calculating the slope of the relative resistance change with respect to the applied tensile strain according to:

$$GF = \frac{\delta(\Delta R / R_0)}{\delta \varepsilon} = \frac{\delta((R(\varepsilon) - R_0) / R_0)}{\delta \varepsilon} = \frac{1}{R_0} \frac{\delta R}{\delta \varepsilon} \quad \text{Eq. (15)}$$

where ε is the mechanical strain applied to the sensor; and R_0 and R are respectively the resistance of the sensor before and after deformation.

Table 1. Processing conditions and the corresponding structural information of SWCNT dispersions used for fabricating SWCNT thin film piezoresistive sensors on PDMS and PET substrates

Sensor Substrate	Dispersion Processing Conditions	Properties of SWCNT bundles in the dispersion			
	Sonication Duration (hrs)	Sedimentation Coefficient ($\times 10^{-12}$ sec)	Diffusion Coefficient ($\times 10^{-8}$ cm ² /sec)	Average Length (nm)	Average Diameter (nm)
PDMS (26 sensors being fabricated by varying the amount of dispersion in spray coating process)	0.5 (1)	140.0	0.53 ± 0.059	5446	22.6
	0.5 (2)	89.3	0.79 ± 0.088	3546	18.4
	4	5.06	2.79 ± 0.12	1039	4.3
	10 (1)	7.57	3.01 ± 0.34	901	5.6
	10 (2)	4.56	3.98 ± 0.38	677	4.2
	50	3.39	4.85 ± 0.42	549	3.7
PET (24 sensors being fabricated by varying the amount of dispersion in spray coating process)	0.5	40.3	0.89 ± 0.14	3330	12.0
	1	38.3	1.11 ± 0.17	2571	11.9
	2	11.2	1.50 ± 0.056	2030	6.2
	4	3.75	2.79 ± 0.12	1074	3.6
	10	3.42	4.79 ± 0.00	557	3.7
	30	1.49	6.20 ± 0.11	447	2.4

Unlike the PET sensor, the relative resistance change of PDMS sensors showed apparently nonlinear responses in the range of the applied cyclic tensile strains (0 – 30%), as shown in Figure 8(b). This suggests that the gauge factor for PDMS sensors depends on the applied strains. For all the PDMS sensors, it was generally observed that the greater is the applied strain, the higher is the gauge factor. In addition, in the range of 20% - 30% tensile strain, the relative resistance change of PDMS sensors showed approximately linear dependence on the applied stain (Figure 8(c)). On the basis of this experimental observation, the gauge factor for PDMS sensors at large deformation was evaluated according to the slope

of a linear fitting of the relative resistance change $\Delta R/R_0$ with respect to the tensile strain in the range (20 % - 30 %).

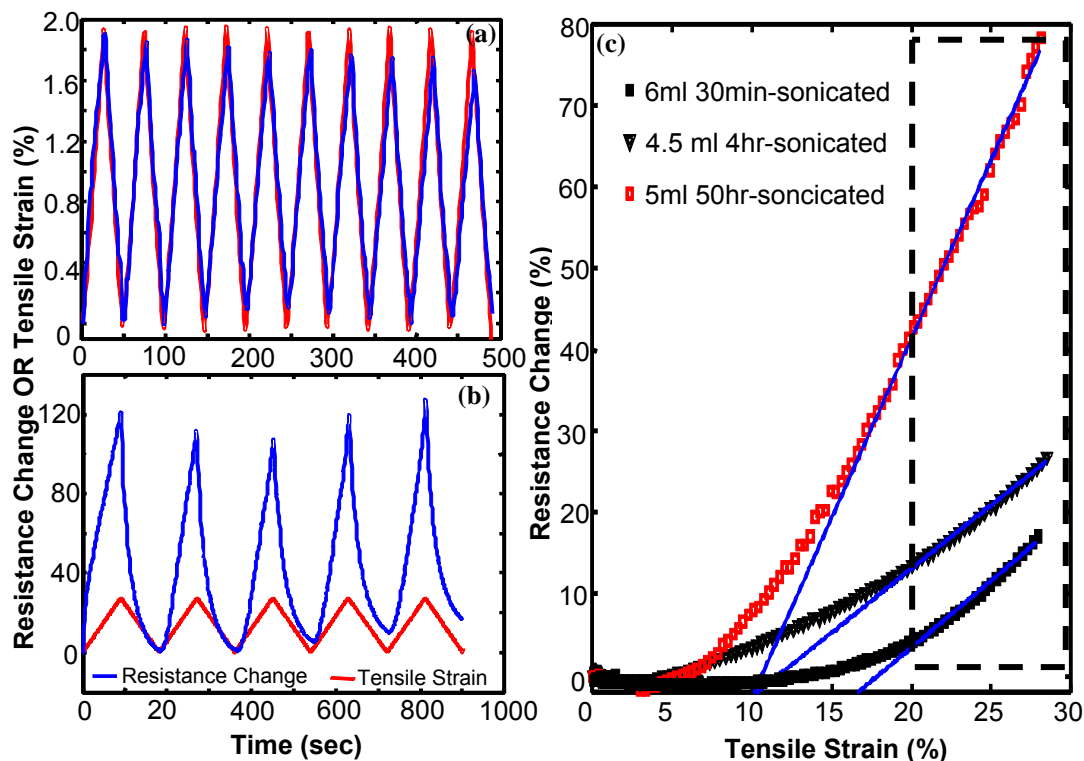


Figure 8. Representative coupled electrical-cyclic tensile testing results for evaluating the sensing performance of SWCNT thin film piezoresistive sensors. (a) PET sensor fabricated by spray coating of 20 ml 2hr-sonicated SWCNT dispersion; (b) PDMS sensor fabricated by spray coating of 10 ml 50hr-sonicated SWCNT dispersion; (c) Gauge factor evaluation of PDMS sensors at large deformation - the slope of a linear fitting (smooth lines) of the relative resistance change $\Delta R/R_0$ with respect to the tensile strain in the range (20 % - 30 %).

According to the evaluation methods described above, the gauge factor for all the sensors (26 PDMS sensors and 24 PET sensors) was calculated. Figure 9 shows the results. The gauge factor data and the associated error bar (one-standard deviation) for each sensor shown in Figure 9 are the averaged results over the multiple tensile testing cycles. The plot of the gauge factor against the optical absorbance at 550 nm allows a study of the effects of film thickness on the sensing performance of SWCNT thin film piezoresistive sensors, since the optical absorbance of SWCNT thin film was linearly proportional to its thickness. The results shown in Figure 9 clearly indicate that the PET sensors do not show thickness-dependent piezoresistive response. Regardless the different sizes of SWCNT bundles in the dispersion that was used for fabricating the sensors, a close to unity gauge factor was obtained for PET sensors at small tensile deformations. Unlike the PET sensors, the PDMS sensors, of which the piezoresistive response was evaluated at large tensile deformation, showed different thickness-dependent behaviors. When the PDMS sensors were fabricated from 30-min and 4hr-sonicated SWCNT dispersion (long and thick SWCNTs), the sensor gauge factor did not show strong

thickness dependence and it was similar to that of PET sensors. Nevertheless, for the PDMS sensors fabricated from 10hr- and 50hr-sonicated SWCNT dispersion (short and thin SWCNTs), their gauge factor manifested strong positive correlations with the film thickness. Moreover, the PDMS sensors fabricated from 50hr-sonicated SWCNT dispersion assumed consistently higher gauge factors than the ones fabricated from 10-hr sonicated SWCNT dispersion. The mechanism(s) for the PDMS sensors to show the thickness-dependent piezoresistive response is not clearly understood. However, the detailed packing structure of SWCNTs in the thin film, as well as its dependence on film thickness and its modification upon large tensile deformation presumably play a critical role.

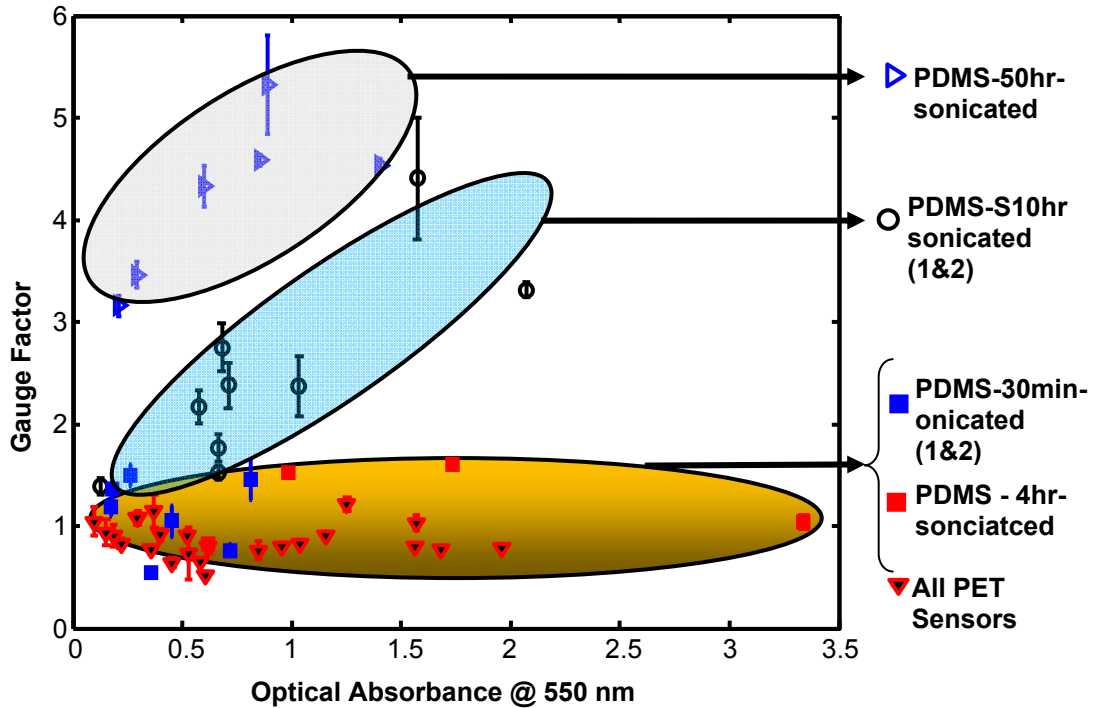


Figure 9. Effect of thin film thickness (optical absorbance) on the gauge factor of SWCNT thin film piezoresistive sensors. Coupled electrical-cyclic tensile testing was used to evaluate the gauge factors of PET sensors in the range of small tensile strain (0 – 2 %) and PDMS sensors in the range of large tensile strain (20% - 30%).

The gauge factor results shown in Figure 9 suggest the compounding effect of film thickness and SWCNT microstructures on the piezoresistive response of SWCNT thin films. To further illustrate the role of SWCNT microstructures, we calculated the average values of the gauge factor for the sensors of different thicknesses but fabricated using the same dispersion method. The results for both PET and PDMS sensors are shown in Figure 10(a), where the thickness-averaged gauge factor is plotted against the SWCNT diffusion coefficient of the corresponding dispersion used for the sensor fabrication. Evidently, by increasing the diffusion coefficient or decreasing the size of SWCNT bundles in the SWCNT dispersion, the gauge factor of the correspondingly fabricated PDMS sensor showed a clearly increasing trend. Figure 10(a) also indicates that, for the PET sensors, the gauge factor dependence on the SWCNT microstructures was rather weak or negligible.

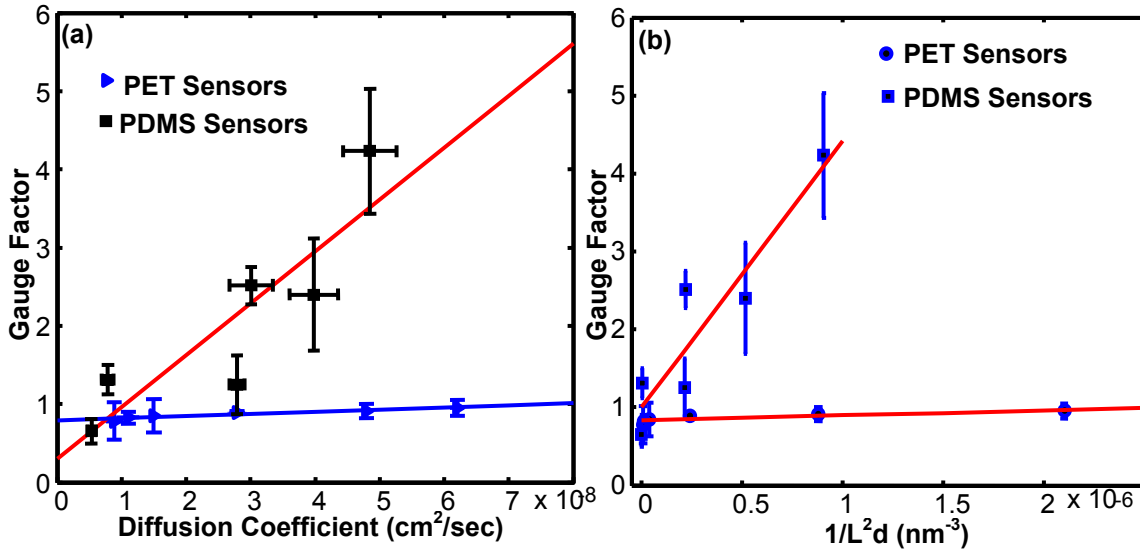


Figure 10. Effects of SWCNT microstructures on the piezoresistive performance of SWCNT thin film sensors. Thickness-averaged gauge factor of SWCNT thin film piezoresistive sensors depended on: (a) the SWCNT bundle diffusion coefficient in the dispersion; and (b) the inverse of the excluded volume of SWCNT bundles, which is proportional to the SWCNT number packing density in the thin film.

The geometric packing problem of thin-rods or fibers has been studied for years [70, 71, 72]. One of the key physical parameters to dictate the packing structure of thin rods is the excluded volume of the rod - V_{ex} , which is approximately given by dL^2 - d is the rod diameter and L is the rod length. The excluded volume refers to the spatial region around a rod that cannot be accessed by the center of mass of another rod. With this definition, one finds that the rod packing density - the number of rods packed in a unit volume in a randomly packed rod ensemble - is proportional to $1/dL^2$. On the basis of this result and using the bulk averaged diameter and length of SWCNT bundles in the dispersion as determined by the PUM and DLS methods, we attempted to understand the relationships between the SWCNT packing density and the gauge factor of SWCNT thin film piezoresistive sensors. Figure 10(b) shows the results. Similar to Figure 10(a), the gauge factor shown in Figure 10(b) is a thickness-averaged result. Again, the critical roles of SWCNT microstructures in dictating the piezoresistive behavior of PDMS sensor for large deformation are evidently shown in Figure 10(b). In contrast to PDMS sensors, the piezoresistive response of PET sensors for small deformation presents only a weak or negligible dependence on the SWCNT microstructures. The microstructure-dependent piezoresistivity of SWCNT thin film sensors being studied here is limited to a finite range of SWCNT bundle size ($447 \text{ nm} \leq L \leq 5446 \text{ nm}$; $2.4 \text{ nm} \leq d \leq 22.6 \text{ nm}$). It will be very interesting if the similar studies are performed for the SWCNTs with even shorter length and diameter. As suggested by the results shown in Figure 10(b), this could lead to SWCNT thin film sensors with even higher gauge factor for large deformation.

The mechanism(s) regarding the piezoresistivity of carbon nanotube (CNT)/polymer nanocomposites have been studied experimentally and numerically [73, 74, 42]. The key factors being identified to dictate the piezoresistive response of CNT/polymer nanocomposites include

[73,74]: 1) the significant variation, e.g., breakage or loss contact, of the conductive paths and network formed by CNTs under applied strains; 2) the change of separation between neighboring CNTs induced alteration of the tunneling resistance; and 3) the intrinsic electrical conductivity change of individual CNTs due to mechanical deformation. Given the similarity of the network structures formed by CNTs in CNT/polymer nanocomposites and those in SWCNT thin films, one expects these previously identified mechanism(s) could also be applicable to SWCNT thin film piezoresistive sensors. Nevertheless, considering the lack of load-transfer medium, i.e., polymer matrix, in SWCNT thin films, we believe the contribution of factor 3) to the piezoresistivity of SWCNT thin film is negligible, since the externally applied mechanical strain/stress cannot be efficiently transferred to the individual tubes to induce their deformation. Instead, it mainly causes the variation of the conductive paths/network formed by SWCNTs as well as the changes of inter-tube (or inter-SWCNT bundle) distance. This leaves the factors 1) and 2) to be responsible for the piezoresistive response of SWCNT thin film sensors. As indicated by the numerical studies in [42], the number of conductive paths in SWCNT thin film expects to increase with the SWCNT packing density ($\propto 1/dL^2$). With this in mind and by noting the results shown in Figure 10 (a) and (b), we further argue that, the piezoresistivity of SWCNT thin film sensors is dominated by factor 2) for both large (PDMS sensors) and small deformation (PET sensors). Otherwise, if the factor 1) were the dominated mechanism, the PDMS sensor should have shown higher gauge factor for smaller SWCNT packing density ($\propto 1/dL^2$), since the number of conductive paths are less in this case and the resistance change of the network is more sensitive to the breakage of conductive paths. Apparently, Figure 10(b) shows the opposite result – the gauge factor of PDMS sensors increases with increasing the SWCNT packing density. On the other hand, the observation shown in Figure 10(b) is consistent with the argument that the factor 2) dictates the piezoresistive response of SWCNT thin film sensors. This is because, at high SWCNT packing density, the size of SWCNT bundles is smaller (short L and thin d), which results in an increase of the number of inter-tube (inter-bundle) contacts/junctions. As a consequence, the ratio of the tunneling resistance to the overall resistance of the thin film increases and it leads to higher piezoresistive sensitivity [73, 74]. In conjunction with the fact that the tunneling resistance has an exponential dependence on the separation of inter-tube (inter-bundle) distance, the same reasoning can also explain that, with increasing the SWCNT packing density, the SWCNT thin film sensors tested for large deformation (PDMS sensors) show significantly improved piezoresistive sensitivity than those tested for small deformation (PET sensors).

4.2.2 Effect of SWCNT orientation

The drastically different piezoresistive behavior of PDMS sensor as compared to that of PET sensor suggests that the SWCNT orientation in the thin film is critical in dictating the piezoresistivity of SWCNT thin film sensors. To this regard, both theoretical simulation and [39,40, 41, 42] experimental research [75, 76] efforts have been devoted to understand the effects of CNT orientation/alignment on the piezoresistive gauge factor of CNT/polymer composite strain sensors. Nevertheless, one finds apparently contradictory findings/conclusions from these previous works. The simulation work by Hu et al. [41] on a 3D CNT network concluded that the sensor sensitivity increases with decrease of the orientation order, because the random distribution of CNT can increase the tunneling resistance locations in a network.

On the contrary, Rahman et al. [39] simulated the piezoresistive response of a 2D CNT network, which suggested that the gauge factor increases with increasing the CNT orientation first and then decreases when the CNTs are highly aligned. The gauge factor increase with CNT orientation has been attributed to the increased tube-tube distance and consequently the tunneling resistance of the CNT network. However, this view is challenged by the simulation work of Ye et al. [40] based on a 3D hard-core model with a soft tunneling shell. It has been found that when a strain is applied, some junctions are enlarged and some are reduced due to lateral deformation. As a consequence, they concluded that, to improve the piezoresistivity of a CNT/polymer composite, it is highly desirable for the CNTs to have a normal orientation to the strain direction. Multiscale simulation studies on 2D and 3D CNT network by Theodosiou et al. [42] also indicated that a high degree of CNT alignment facilitates the piezoresistive sensitivity of CNT/polymer composites, but for a different reason. In their study, the intrinsic piezoresistivity of CNTs rather than the tunneling resistance was attributed as the major contribution to result in the resistance change of the composite. However, a recent similar multi-scale simulation study on 3D CNT network by Hu et al. [43] argued that, as compared to the tunneling resistance and network breakage, the contribution of intrinsic piezoresistivity of CNTs is limited.

Given the progress being made, however, there is still a lack of experimental studies to systematically vary and quantify the degree of orientation of CNTs and understand their effects on the piezoresistivity of CNT based strain sensors. In this project, we made use of spray coating technique to fabricate thin films of SWCNTs on polyethylene terephthalate (PET) film. Subsequent mechanical stretching of the PET substrate to different draw ratio at an elevated temperature allowed for the fabrication of oriented SWCNT thin films with varied degrees of orientation, of which the corresponding piezoresistivity was then evaluated by the coupled electrical-mechanical tests. With assistance of polarized Raman spectroscopy and scanning electron microscopy, the orientation order and morphologies of the stretched SWCNT thin films were quantitatively and qualitatively evaluated. Such acquired systematic results ultimately lead to a quantitative relationship between SWCNT alignments and piezoresistive gauge factors, which expect to be useful for gaining further insightful understanding of the effects of CNT orientation/alignment on the piezoresistive behavior of CNT based strain sensors.

The piezoresistive behaviours of the SWCNT thin films of different draw ratios were evaluated by measuring the change in electrical resistance upon the application of a cyclic tensile strain. Figures 11a and 11b show the representative piezoresistive response of the unstretched ($\lambda = 1$) and the stretched ($\lambda = 3.2$) S2hr SWCNT thin films, respectively. Clearly, the piezoresistivity or resistance-strain behaviour for both the stretched and unstretched SWCNT thin films show good linearity, repeatability and stability, which is essential for their use as reliable strain sensors/gauges.

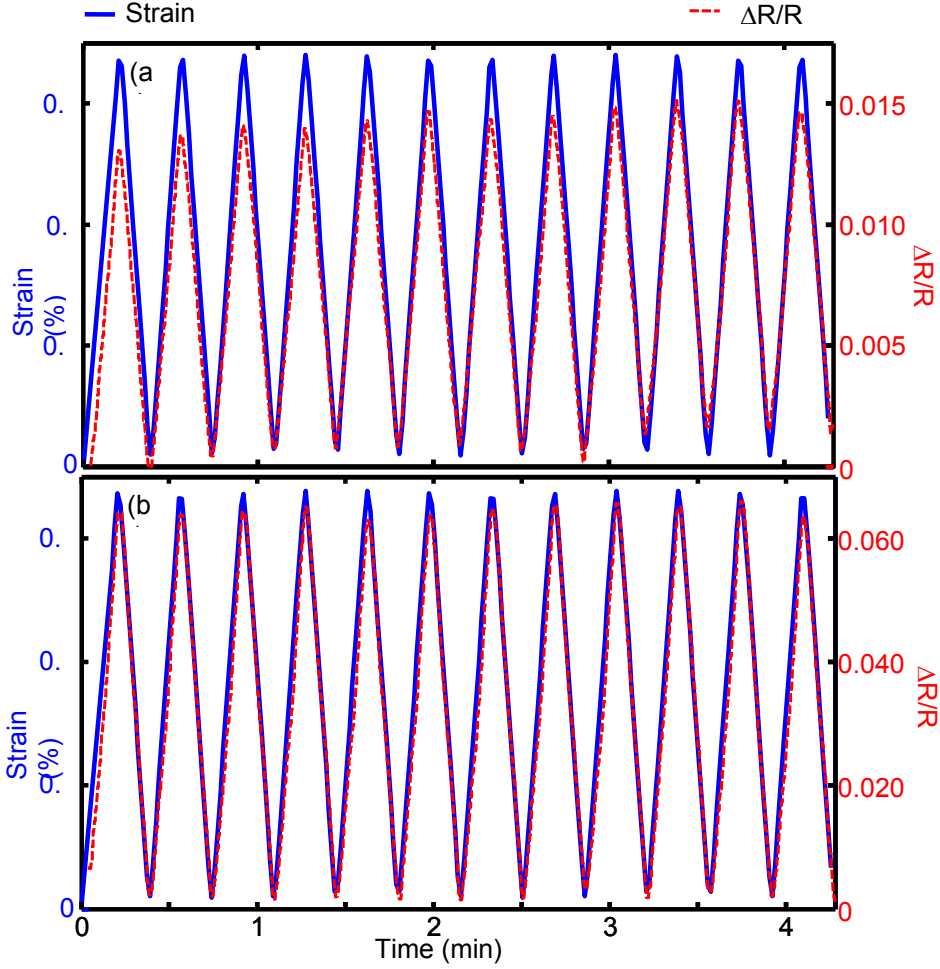


Figure 11. Relative changes in electrical resistance for S2 hr SWCNT thin films under cyclic tensile test. (a) Unstretched thin film with draw ratio $\lambda = 1.0$; and (b) Stretched thin film with draw ratio $\lambda = 3.2$.

Figure 12 compares the GF results for both S2hr and S10hr thin films at different draw ratios. Within the experimental errors, there is a clear positive correlation between the draw ratio and gauge factor for both S2hr and S10hr SWCNT thin films. The gauge factor increases by $\sim 6\times$ for S2hr thin films from the unstretched ($\lambda = 1$, $GF = 1.30 \pm 0.14$) to the highly stretched ($\lambda = 3.2$, $GF = 7.19 \pm 4.76$). A similar $\sim 3\times$ increase of the GF upon stretching for S10hr SWCNT thin film was also observed ($GF = 1.47 \pm 0.53$ for $\lambda = 1$ and $GF = 4.70 \pm 1.63$ for $\lambda = 3.2$). Within the experimental error, the results shown in Figure 12 also indicate that, the stretched S2hr SWCNT thin films have higher gauge factors as compared to S10hr samples. It is especially the case for high draw ratio samples. This suggests that the CNTs with larger diameter could facilitate the sensitivity enhancement when considering that the diameter of SWCNT bundles in S2hr thin films is greater than that in S10hr thin films. The experimental observation here agrees with the numerical simulations results reported in [40] but is in contradictory to that disclosed in [41]. As argued in [41], the smaller diameter of CNTs results in a reduced tunnel area that leads to a

higher tunneling resistance and therefore high piezoresistive sensitivity. In contrast, the work in [40] identified that the average junction gap variation increases with the CNT diameter. As a consequence, the larger diameter of CNTs can lead to a higher tunneling resistance change and therefore high piezoresistive sensitivity. The contradictory prediction in [40] and [41] on the effect of CNT diameter seems to originate from the negligence of the 3D nature of the tube-tube junction. In the former case, the 2D aspect of the junction (tunnel area) was emphasized; and in the latter case, the 1D aspect of the junction (junction gap) was considered. Further investigations, both experiments and simulations, are necessary to clarify this outstanding issue.

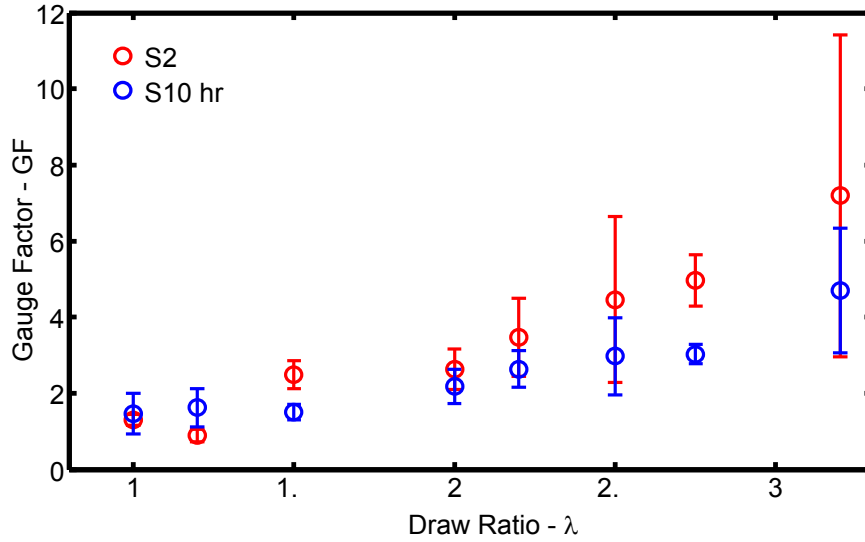


Figure 12. Effect of mechanically drawing on the gauge factor of S2hr and S10hr SWCNT thin films.

Regardless of the effect of SWCNT bundle diameter, the positive correlation between the draw ratio and the gauge factor of SWCNT thin films shown in Figure 12 is consistent with the experimental findings previously reported in [31, 75, 76]. That is, the CNT alignment has a profound effect on the sensitivity of CNT based strain sensors. The higher degree is the CNT alignment, the higher is the gauge factor. As discussed next, this qualitative effect can be further understood by quantifying the degree of CNT orientations and establishing its relationship to the piezoresistive sensitivity of SWCNT thin films.

According to [50] and considering the 2D uniaxial planar orientation of SWCNTs in a mechanically-drawn SWCNT thin film, we can correspondingly derive the polarized Raman intensity for both VV and VH configurations as following:

$$I_{SWCNT}^{VV}(\Phi) \propto \int_{-\pi/2}^{\pi/2} f(\theta) [\cos \theta \cos \Phi - \sin \theta \sin \Phi]^4 d\theta \quad \text{Eq. (16a)}$$

$$I_{SWCNT}^{VH}(\Phi) = \int_{-\pi/2}^{\pi/2} f(\theta) [\cos \theta \cos \Phi - \sin \theta \sin \Phi]^2 [\cos \theta \sin \Phi + \sin \theta \cos \Phi]^2 d\theta \quad \text{Eq. (16b)}$$

where θ and Φ are the angle formed between the drawing direction and a SWCNT and the polarization direction of the incident laser beam, respectively. $f(\theta)$ is the orientation distribution function of SWCNTs in the thin film. The wrapped Cauchy distribution [77,78,79] has been successfully used for describing the orientation distribution of a quasi-2D fiber network, e.g., paper. Considering the structural similarity between SWCNT thin film and paper, we herein use the same function:

$$f(\theta) = \frac{(1 - S^2)}{\pi(1 + S^2 - 2S \cos(2\theta))} \quad \text{Eq. (16c)}$$

to approximate the SWCNT orientation distribution in the mechanically-drawn SWCNT thin films. In Eq. (16c), S is the orientation order parameter. It takes a value of 0 for a random distribution and 1 for a perfectly oriented SWCNT thin film. With the help of Eq. (16a-16c), one can fit the experimentally collected Raman spectra in VV and VH configuration to readily determine the order parameter S for a given SWCNT thin film sample. The results of S for both S2hr and S10hr thin films plotted against the draw ratio are shown in Figure 13. Within the experimental error, it seems that, at the same draw ratio, there is no significant difference of the order parameters for S2hr and S10hr SWCNT thin films. Moreover, one can clearly identify a logarithmic increase of the order parameter S with the draw ratio. An empirical relation of $S = 0.475 \ln \lambda$ provides a nice fitting to quantify the order parameter of a mechanically drawn SWCNT thin film at draw ratio λ . This relation along with the positive correlation between λ and GF as observed in Figure 12 once again confirm that, with increasing the degree of SWCNT alignment, the piezoresistive sensitivity of SWCNT thin film increases.

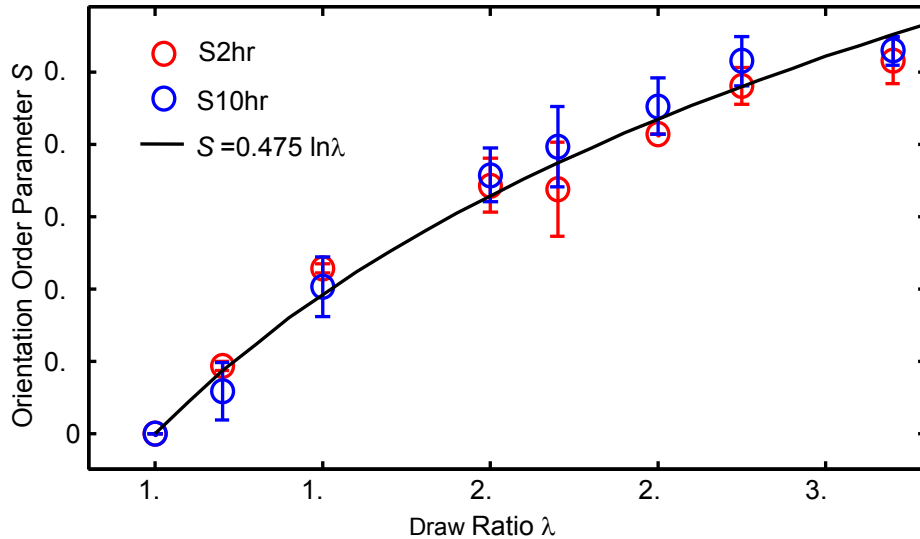


Figure 13. The orientational order parameter S for the mechanically-drawn SWCNT thin films at varied draw ratios.

The mechanically drawing would cause an area increase of the SWCNT thin film and therefore a decrease of the SWCNT packing density/areal density. This point can be understood by considering that the SWCNT thin film deforms coincidentally with the substrate

PET. Let λ_x , λ_y , and λ_z be respectively the draw ratio of the PET substrate in the direction of through-thickness, in-plane transverse, and mechanical drawing. If there is no slippage, the draw ratio for SWCNT thin film in the direction of in-plane transverse and mechanical drawing should be the same as λ_y and λ_z . In uniaxial stretching ($\lambda_x = \lambda_y$) and assuming there is no volume change of PET, which is a quite reasonable assumption, we have $\lambda_z \lambda_y^2 = 1$. With this relation, we can readily arrive at Area (λ)/Area ($\lambda=1$) = $\lambda_z \lambda_y = \lambda_z^{0.5}$. Since $\lambda_z \geq 1$, we have an increased thin film area upon drawing. As a consequence, the contribution of tunneling resistance in the stretched thin film becomes more important due to the directional alignment of SWCNTs as well as the reduced areal density. Since higher sensitivity of CNT based piezoresistive sensor is associated with increasing tunneling resistance, this explains the high gauge factors of the mechanically stretched SWCNT thin films at higher draw ratios. In addition to alignment and areal density reduction, the stretching induced morphology changes and even breakage of SWCNT network is also considered to be critical in responsible for the significantly increased sheet resistance and the corresponding tunneling resistance contribution. To show this point, Figure 14 compares the SEM images of the S2hr SWCNT thin films at different draw ratios. The unstretched SWCNT thin film ($\lambda = 1.0$) is featured by a randomly entangled SWCNT bundles/ropes. The densely packed SWCNT network results in a large number of intimate SWCNT-SWCNT contacts/junctions and the related conductive pathways to give high electrical conductivity or low sheet resistance. With increasing the draw ratio to $\lambda = 1.2$ and $\lambda = 1.5$, the alignment of the SWCNT rope/bundles in the drawing direction becomes apparent. At this stage, the integrity of the entangled SWCNT network is maintained. Upon stretching the thin film to $\lambda = 2.0$, one can clearly visualize the formation of slender microcracks that orients perpendicularly to the drawing direction. With further increasing the draw ratio ($\lambda = 2.2, 2.5, 2.75$, and 3.2), the microcracks, in terms of both number and size, gradually grow and connect to each other to lead to the thin film an “island-bridge” structures. The SWCNTs in the “island” has a less degree of alignment and packing density than those in the “bridge” region. In order for the charge carriers to transport through the SWCNT thin film, they have to take the “bridge” route, where the SWCNT-SWCNT contacts/junctions are significantly reduced due to the high degree of alignment and low packing density. As a consequence, the charge transport in the highly drawn SWCNT thin films is dominated by tunneling, which results in the significantly higher sheet resistance and high piezoresistive sensitivity.

4.3 Hybrid approach to tailor the sensing characteristics of SWCNT thin films

In the application of different types of piezoresistive sensors, e.g., the most widely used bonded metallic strain gage, due to the temperature-dependent electrical resistance of the sensing materials, the temperature compensation has to be appropriately carried out in order to accurately determine the strain/stress levels being measured. [80] This is typically done by recording the resistance of two identical sensors – one is under strain and the other is free from deformation. Like the other strain gages, the SWCNT thin film piezoresistive sensors are not immune from temperature compensation, since the electrical resistance of SWCNTs is temperature dependent [81]. Nevertheless, by recognizing the different electronic transport behaviors in graphite nanoplatelets (GNP) and SWCNT thin films – the former (latter) is metallic (semi-conductive) and has positive (negative) temperature coefficient of resistance, we were able to fabricate SWCNT/GNP hybrid thin films capable of self-temperature compensation.

Upon a wise selection of the ratio of SWCNTs to GNPs, we achieved very low (near zero) temperature coefficients of resistance in a broad temperature range for SWCNT/GNP hybrid thin film piezoresistive sensors. This unique self-temperature compensation feature and high sensitivity ($GF \sim 8.0$) of SWCNT/GNP hybrid thin film piezoresistive sensors provides them a vantage for readily and accurately measuring the strain/stress levels in different conditions.

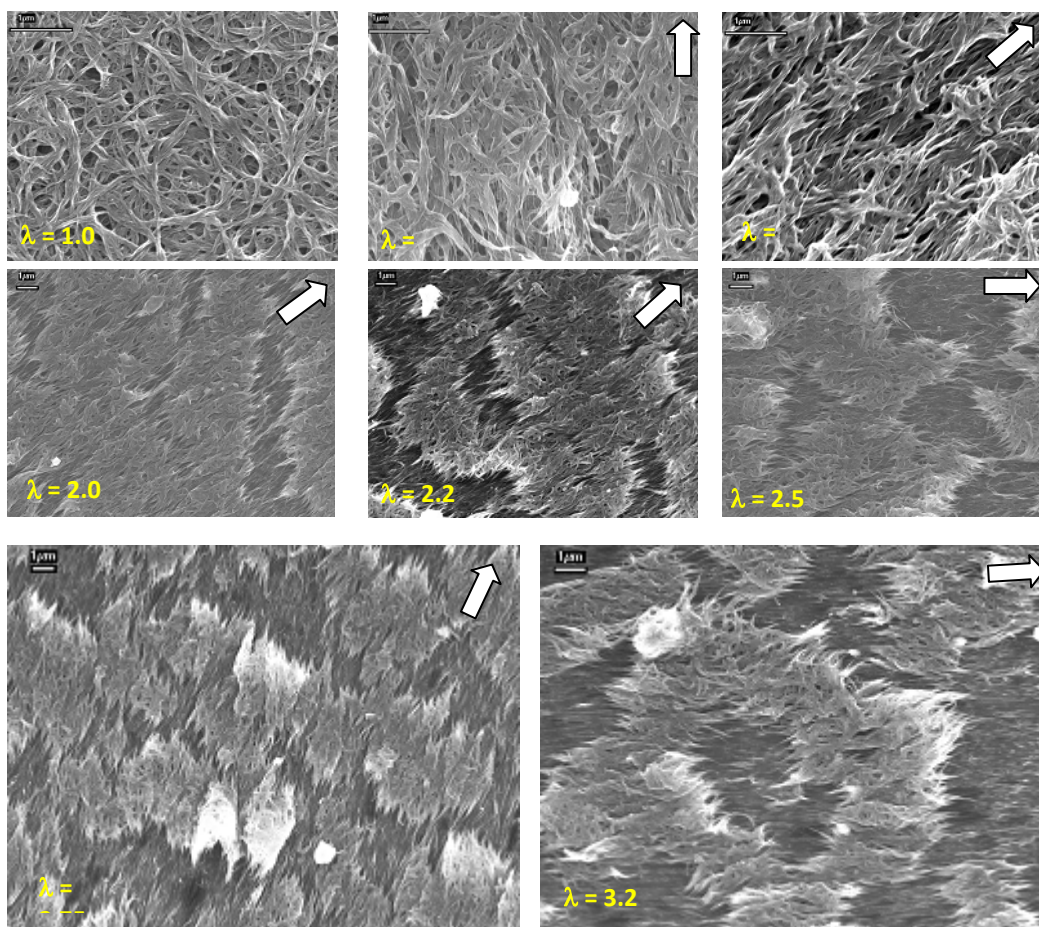


Figure 14. SEM images of the mechanically drawn S2hr SWCNT thin films to show the stretching induced morphological changes of SWCNT network. All the scale bars are for 1 μ m. The arrow indicates the stretching direction.

To fabricate SWCNT/GNP hybrid thin films, the SWCNT and GNP aqueous dispersions were prepared first with sonication process assisted by an anionic surfactant - sodium dodecylbenzenesulfonate (SDBS) by following the procedures as detailed in Experimental section. The typical composition of SWCNT dispersion includes 0.016 wt. % of SWCNTs and 0.7 wt. % of SDBS; and the typical composition of GNP dispersion includes 0.3 wt. % of GNPs and 0.07 wt. % of SDBS. With the as-sonicated SWCNT and GNP dispersions, a spray coating technique was carried out to fabricate SWCNT/GNP hybrid thin films. In brief, a fixed amount of SWCNT dispersion (0.25 ml) was first deposited onto a 4 cm \times 4 cm polyethylene terephthalate (PET) substrate with temperature controlled at 90 $^{\circ}$ C to facilitate water evaporation. Subsequent to the deposition of SWCNT dispersion, the as-formed SWCNT thin film was further

subjected to an immersion treatment in deionized water for 2hr and then dried in air. The immersion-drying treatment allows for the removal of residual SDBS molecules and form compact thin film structures [31]. After the layer of SWCNT thin film was formed, a specified amount of GNP dispersion was then further deposited by following the same procedures for hybrid thin film formation. By varying the amount of GNP dispersion from 0.125 to 8 ml, we obtained SWCNT/GNP hybrid thin films covering a broad range of mass ratio of SWCNT to GNP (0.00167 to 0.107) at different film thickness. For comparison, neat SWCNT and GNP thin films were also prepared by the similar procedures. Fig. 15a shows the optical photographs of the neat SWCNT, GNP, and a representative SWCNT/GNP hybrid thin film samples. The transparent/translucent nature of these films qualifies their “thin” characteristics. The translucent appearance of GNP and SWCNT/GNP hybrid thin films is due to the strong scattering of the relatively large sized GNPs (microns in lateral dimension) to the visible light. The SEM images of the neat SWCNT and GNP thin film respectively shown in Fig. 15b and 15c clearly reveal the SWCNT rope/bundle entangled network structures in the former and the stacked mosaic morphologies of GNP platelets in the latter. Fig. 15d and 15e respectively show the SEM and AFM images of the SWCNT/GNP hybrid thin film. Both images clearly reveal the mixed structures of SWCNT entangled network and GNP mosaic platelet stacks in the hybrid film. With AFM imaging, we roughly estimated the lateral dimension (~ 1000 nm) and the thickness of GNPs (a few nanometers).

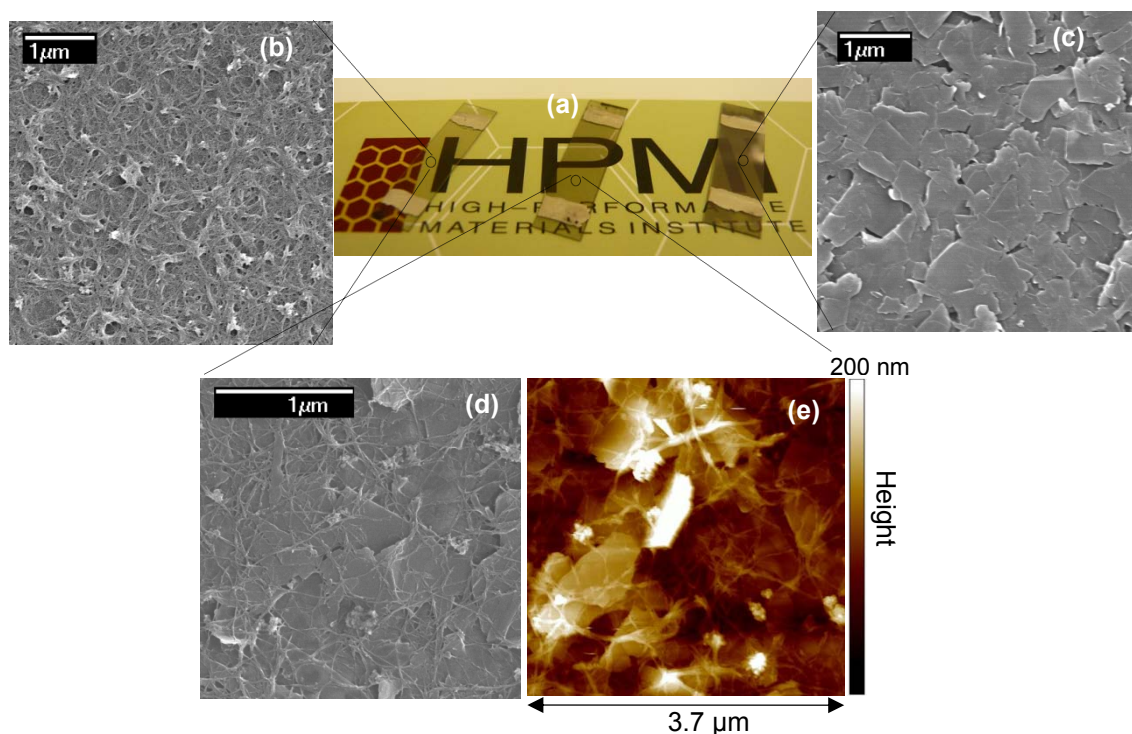


Figure 15. (a) Optical photographs of neat SWCNT thin film (left), SWCNT/GNP hybrid thin film (middle), and neat GNP thin film (right) piezoresistive sensors; (b) SEM image of neat SWCNT thin film; (c) SEM image of neat GNP thin film; (d) and (e) SEM and AFM image of SWCNT/GNP hybrid thin film.

Fig. 16a and 16b respectively show the sheet resistance and gage factor of SWCNT/GNP hybrid thin films with respect to the amounts of GNPs used for film fabrication. In the same figure, the results of neat GNP thin films are also shown for comparison. It is evident in Fig. 16a that, even with an inclusion of small amounts of SWCNTs, the sheet resistance of SWCNT/GNP hybrid film is significantly reduced as compared to that of neat GNP films. Associated with the sheet resistance reduction, the gage factor of SWCNT/GNP hybrid film (Fig. 16b) is accordingly decreased when compared to that of the neat GNP film. The more SWCNTs being included, the less sensitive is the piezoresistive response of the SWCNT/GNP hybrid film. By varying the mass ratio of SWCNTs to GNPs from 0.00167 to 0.107, the GF of SWCNT/GNP hybrid film is accordingly decreased from 7.8 ± 0.25 to 4.0 ± 0.31 . The effect of inclusion of SWCNTs in SWCNT/GNP hybrid film to reduce its sheet resistance and piezoresistive sensitivity is believed to be a consequence of mixing rule – a balanced result of the high electrical conductivity and low gage factor of SWCNT network and the low electrical conductivity and high gage factor of GNP platelet stacked structures.

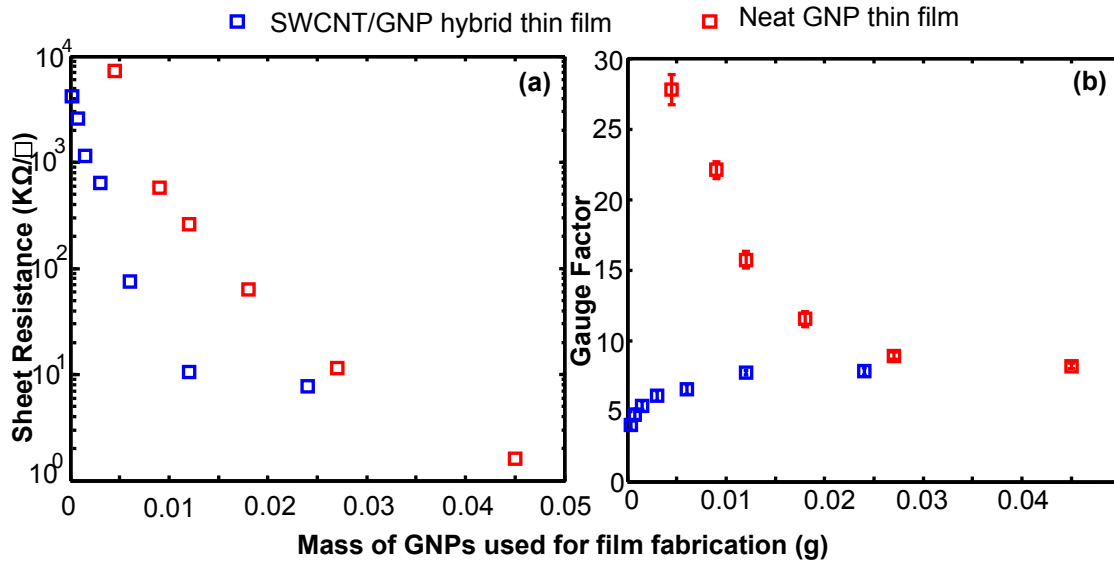


Figure 16. Relationships between the GNP mass used for film fabrication on (a) sheet resistance and (b) gauge factor of neat GNP thin film and SWCNT/GNP hybrid thin film piezoresistive sensors. The SWCNT mass is kept constant – 4.0×10^{-5} g in SWCNT/GNP sensors.

Temperature compensation is necessary in order for the piezoresistive sensors, e.g., bonded metallic strain gage, to given accurate and reliable strain/stress measurement results [80]. Due to their temperature-dependent electrical resistance, this is also true for neat SWCNT or GNP thin film piezoresistive sensors. Fig. 17a shows the temperature ramping results for the selected neat SWCNT and GNP thin film piezoresistive sensors when they were subjected to a sinusoidal displacement signal with the amplitude and oscillating frequency respectively set at 6 μm and 0.2 Hz. Clearly, in the temperature range being tested (30 °C – 85 °C), the neat GNP thin film shows positive temperature coefficient (PTC) of resistance – the sheet resistance increases with increasing the temperature. In contrast to GNP thin film, the neat SWCNT thin film shows negative temperature coefficient (NTC) of resistance – the sheet resistance decreases with

increasing the temperature. The PTC effect of neat GNP thin film is attributed to the metallic nature of GNPs. When temperature increases, due to the enhanced phonon/charge carrier scattering, the mean free path of charge carriers in GNPs is reduced and it causes a decreased mobility and therefore an increased electrical resistance. The NTC effect of neat SWCNT thin film is a result of its semi-conductive charge transport behavior. Previous studies [81,82,83] have shown that the charge transport in SWCNT thin films is dictated by a variable-range hopping mechanism, which facilitates the charge carrier mobility and reduces the resistance at high temperature. Considering the opposite effect of increasing temperature on the electrical resistance of neat SWCNT and GNP thin films, we expect the PTC of GNPs and the NTC of SWCNTs could be compensated in SWCNT/GNP hybrid thin films to result in the unique self-temperature compensation property. Furthermore, if the mass ratio of SWCNT to GNP is appropriately controlled, one may obtain the SWCNT/GNP hybrid thin film piezoresistive sensors with negligible temperature coefficient of resistance. This hypothesis was confirmed by the temperature ramping test of the SWCNT/GNP hybrid thin film sensors. The results are shown in Fig. 17a. As shown in Fig. 17a, by selecting the mass ratio of SWCNT to GNP to be 0.0033, we were able to fabricate the SWCNT/GNP hybrid thin film piezoresistive sensor with close-to-zero temperature coefficient of resistance. The temperature ramping tests were also performed for the other SWCNT/GNP thin film piezoresistive sensors. For comparison, in the same figure, we showed the temperature ramping results for two representative SWCNT/GNP hybrid thin film sensors with the mass ratio of SWCNT to GNP respectively controlled at 0.0016 and 0.0066. As expected, when the mass ratio of SWCNT to GNP is less than 0.0033, the sensor shows PTC effect; and when the mass ratio of SWCNT to GNP is greater than 0.0033, the sensor shows NTC effect.

At the nano- and microscopic length scale, the structure/morphology of SWCNT/GNP hybrid thin film is formed by random packing of SWCNT and GNP particles. The granular/particular nature of such thin films implies that, when charge carriers transport in the film, they must traverse through both SWCNT and GNP domains. As a consequence, we expect that the mass ratio of SWCNT to GNP is a critical factor to dictate the self-temperature compensation property of the SWCNT/GNP hybrid thin film sensors. On the contrary, the deposition sequence of SWCNT and GNP in the formation of SWCNT/GNP thin film is not important. To verify this point, we fabricated SWCNT/GNP hybrid thin film sensor on PET substrate by 1) depositing GNP first then SWCNT and 2) depositing a mixture of SWCNT and GNP dispersion. In both cases, the mass ratio of SWCNT to GNP was controlled at 0.0033. Fig 17b compares the temperature-dependent piezoresistive response of SWCNT/GNP hybrid thin film sensors thus fabricated. Clearly, regardless the film deposition method, the self-temperature compensation has been achieved for all the SWCNT/GNP hybrid thin film sensors. This result confirms that, to have the self-temperature compensation property for SWCNT/GNP hybrid thin film sensor, the key is to control the mass ratio of SWCNTs to GNPs. Certainly, to have a complete understanding of the self-temperature compensation behavior of the SWCNT/GNP hybrid thin films, a further systematic and in-depth study is required to clarify the roles of some other factors, such as, size, shape, and their distribution, detailed packing structures, and chemical functionalization of SWCNT and GNP particles in the hybrid thin films.

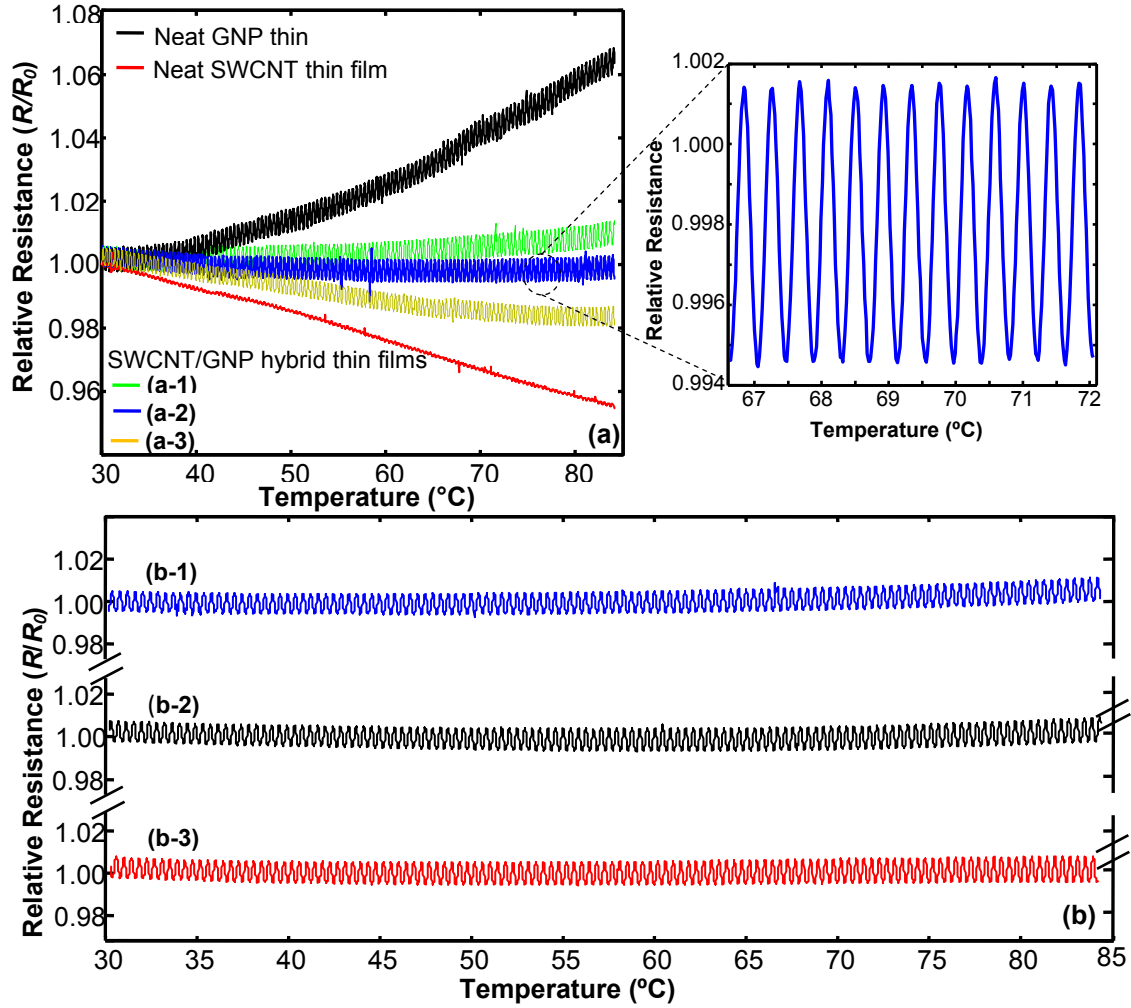


Figure 17. (a) Comparison of the temperature effect on the piezoresistive response of neat GNP thin film (prepared with 15 ml GNP dispersion), neat SWCNT thin film (prepared with 2 ml SWCNT dispersion), and SWCNT/GNP hybrid thin film sensors (prepared with 0.25 ml SWCNT dispersion and (a-1) 8 ml GNP dispersion, mass ratio of SWCNT to GNP equals to 0.0016; (a-2) 4 ml GNP dispersion, mass ratio of SWCNT to GNP equals to 0.0033; and (a-3) 2 ml GNP dispersion, mass ratio of SWCNT to GNP equals to 0.0066). With temperature ramping from 30 $^{\circ}\text{C}$ to 85 $^{\circ}\text{C}$ at a rate of 5 $^{\circ}\text{C}/\text{min}$, a sinusoidal displacement signal (6 μm in amplitude, 0.2 Hz in frequency) was applied for coupled electrical-mechanical test. (b) Self-temperature compensation of SWCNT/GNP hybrid thin films sensors fabricated by: (b-1) depositing SWCNT first then GNP; (b-2) depositing GNP first then SWCNT; (b-3) depositing a mixture of SWCNT and GNP dispersion. In all three cases, the mass ratio of SWCNT to GNP was controlled at 0.0033.

4.4 SWCNT-FibSen fiber sensors for life-long structural health monitoring of polymeric composites - from manufacturing, utilization to failure

4.4.1 Structural characterization of SWCNT-FibSen sensors

With the in-house developed continuous spraying coating process, we have successfully fabricated SWCNT-FibSen sensors on different types of fiber substrates, which included glass

fiber, polyaramid fiber, nylon fiber, and polyethylene terephthalate (PET) fiber. Herein, we focus on SWCNT-FibSen sensors formed on a single filament of glass fiber. Figure 18a shows the optical photographs of the bare glass fiber bundles and the corresponding SWCNT coated SWCNT-FibSen sensor. The dark visual appearance of the SWCNT-FibSen is an indication of a thin layer of SWCNT dense coating formed on the fiber surface, which was corroborated by SEM imaging examination as shown in Figure 18b (low magnification) and Figure 18c (high magnification). Albeit its small diameter ($\sim 20\mu\text{m}$), the SWCNT thin film formed on the glass fiber has the similar rope/bundle entangled network morphologies as the one deposited on a large-area 2D substrate [31].

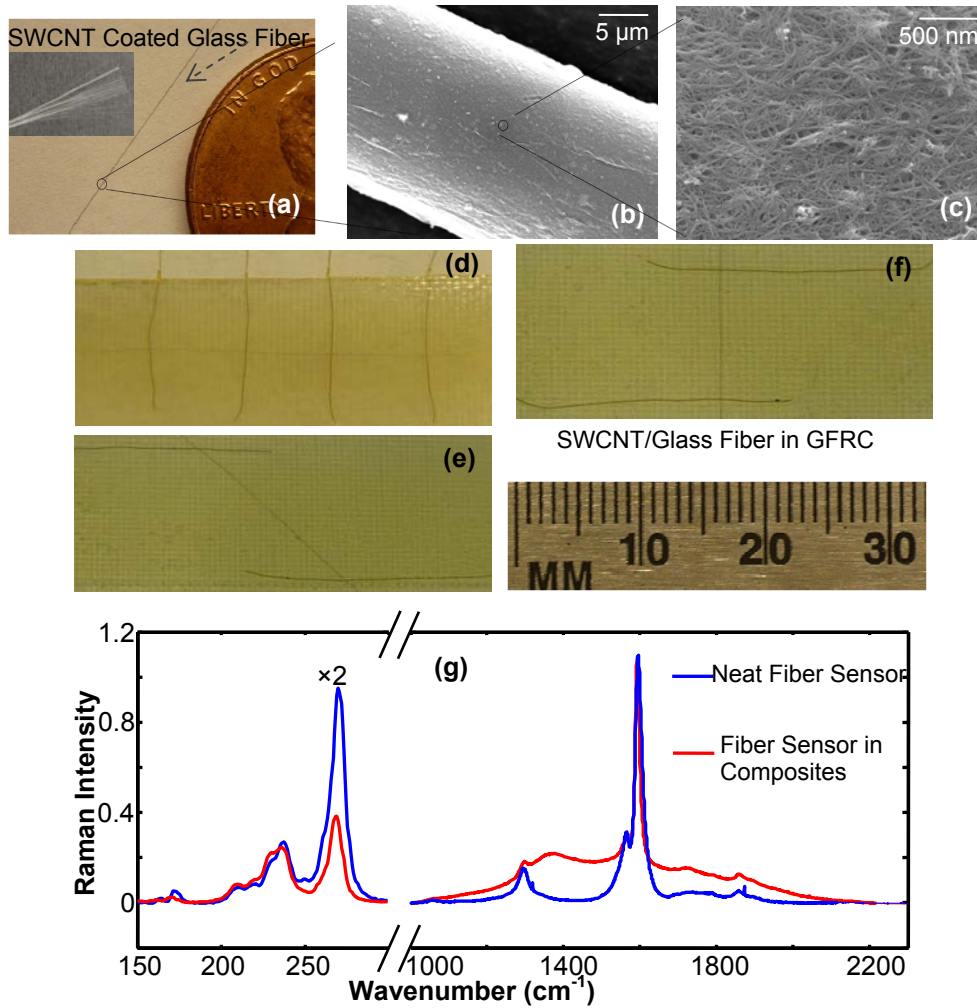


Figure 18. (a) Optical photographs of neat glass fiber (inset) and the corresponding SWCNT thin film coated glass SWCNT-FibSen sensor; (b) and (c) SEM images of glass SWCNT-FibSen sensor at low and high magnification, respectively; (d), (e), and (f) Optical photographs of epoxy/glass fiber composite laminates embedded with glass SWCNT-FibSen sensor that is respectively oriented at 0°, 45°, and 90° with respect to the tensile loading direction of the specimen; (g) Comparison of the Raman scattering spectra of the standalone glass SWCNT-FibSen sensor and the one embedded in epoxy/glass fiber composite laminate. G-band (1595 cm^{-1}) was used to normalize the spectra; and the RBM bands (150 cm^{-1} – 300 cm^{-1}) were scaled by 2x for clarity.

The SWCNT-FibSen sensors are compatible with the commonly used prepreg techniques for readily manufacturing polymeric composites with self-sensing capabilities. To demonstrate this point, the fiber sensor prepared previously was manually sandwiched between two layers of fiberglass prepreps. Fine gold wire electrodes (50 μ m in diameter) were also incorporated into prepreps for electrical and piezoresistive test/evaluation. A subsequent vacuum bag/hot plate curing process was applied to fabricate SWCNT-FibSen enabled glass fiber reinforced composite (GFRC) coupons. Figure 18d – 18f shows the optical photographs of the representative GFRC coupons, in which the embedded SWCNT-FibSen sensor was respectively oriented at 0°, 45°, and 90° with respect to the long axis of the coupon. Raman spectroscopy was applied to examine the impact of the composite manufacturing process on the chemical structures of SWCNT-FibSen sensors. Figure 18g compares the Raman spectra of a SWCNT-FibSen sensor before and after embedding and curing process. Clearly, the key Raman features of SWCNTs - RBM bands between 150 – 300 cm⁻¹, G-band at 1595 cm⁻¹, and D-band around 1295 cm⁻¹ were preserved upon the manufacturing process [84], which indicates the curing process has minimal impact to induce chemical structure changes of SWCNT-FibSen sensors. One also notes the significant intensity suppression of the RBM band for the embedded SWCNT-FibSen sensor. This is caused by the pressure originated from the cohesive energy of the epoxy matrix that is applied to SWCNTs to restrain their radial breathing vibration mode [85, 86].

4.4.2 In-situ resin curing monitoring of polymeric composites

During the composite manufacturing process, the real-time resistance change of the embedded SWCNT-FibSen sensors is able to provide valuable insights to reveal the resin curing process. To demonstrate this point, the laminates of fiberglass prepreps respectively embedded with glass, polyaramid and nylon based SWCNT-FibSen sensors were subjected to a common curing and thermal aging process, which includes three stages: 1) temperature ramping from 25 – 143 °C; 2) isothermal at 143 °C for 2 hrs; 3) thermal aging with two cooling-heating cycles between 30 °C and 143 °C. Regardless of the different fiber substrates and initial sensor resistance, the general features of these three processing stages were faithfully captured by the real-time resistance change of the SWCNT-FibSen sensors. The results are shown in Figure 19.

As shown in Figure 19, when the temperature ramped from 25 °C to 143 °C during stage 1, a rapid resistance increase of the SWCNT-FibSen sensor was accordingly observed. The resistance increase was as high as 9.5 ×, 11.8 ×, and 12.2 × respectively for glass, polyaramid, and nylon SWCNT-FibSen sensors. In the subsequent isothermal stage (stage 2), the sensor resistance initially manifested a decrease then gradually approached to a stabilized value at the end of stage 2. With a comparison of different types of SWCNT-FibSen sensors, there is a positive correlation of the resistance change between the initial decrease at the beginning of stage 2 and the rapid increase during stage 1. In the cyclic thermal-aging of stage 3, the sensor resistance accordingly followed the temperature cycling sequence, and it increased in the cooling cycle and decreased in the heating cycle. The resistance change of the embedded SWCNT-FibSen sensors reflects the corresponding physical state changes of the resin matrix in the composite manufacturing process. In stage 1, the resin viscosity decreases with temperature ramping. This allows the resin molecules to readily penetrate/infiltrate into the SWCNT network to result in its expansion and even breakage of tube/tube contacts. As a result,

the sensor resistance shows a significant increase. With the proceeding of the curing process, the cross-linking density increases to cause a drastic increase of the system viscosity as well as the matrix shrinkage [87]. Consequently, the resin infiltrated SWCNT network accordingly shrinks to cause the sensor resistance decrease at the beginning of stage 2. During the isothermal of stage 2, the cross-linked resin network is fully developed to stabilize the sensor resistance. In the thermal-aging stage 3, the intrinsic negative temperature coefficient (NTC) of resistance of SWCNT network dominates the sensor resistance behavior. [32,81] In the cooling cycle, the resistance increases; and in the heating cycle, the resistance decreases. Certainly, the thermal expansion of the fully cured laminates could also contribute to the sensor resistance change in stage 3. However, due to the relatively small thermal expansion coefficient of fully cured epoxy/glass composite (~ 20 ppm/ $^{\circ}\text{C}$), this effect is negligible as compared to the intrinsic NTC effect of SWCNT network.

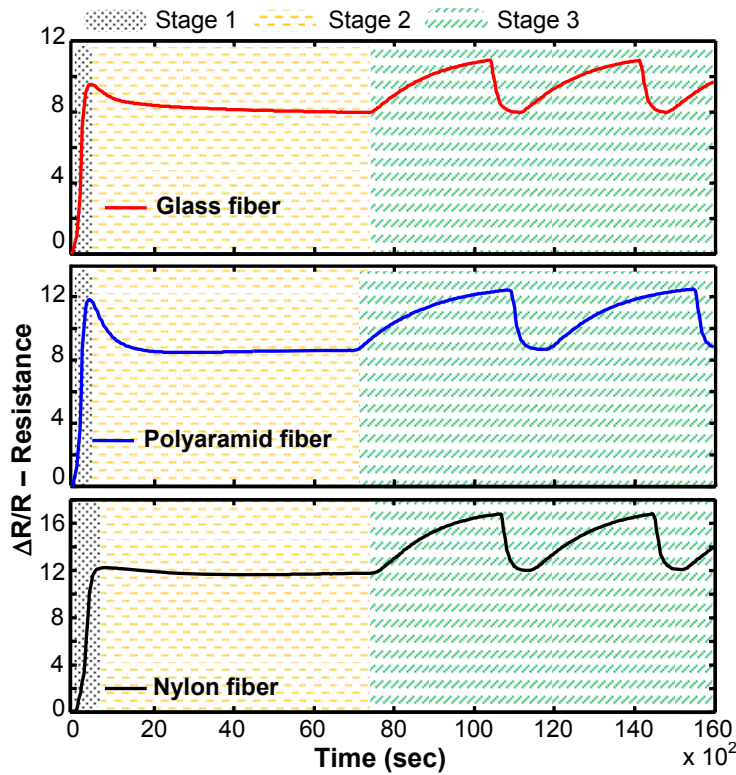


Figure 19. Resin curing process of the epoxy/glass fiber composite registered by the real-time resistance change of different types of SWCNT-FibSen sensors (glass, polyaramid and nylon). Stage 1: temperature ramping from 25 $^{\circ}\text{C}$ to 143 $^{\circ}\text{C}$; Stage 2: isothermal at 143 $^{\circ}\text{C}$ for 2 hrs; Stage 3: cyclic thermal aging – cooling from 143 $^{\circ}\text{C}$ to 30 $^{\circ}\text{C}$ and reheating from 30 $^{\circ}\text{C}$ – 143 $^{\circ}\text{C}$ twice.

The results shown in Figure 19 suggest the great potential of SWCNT-FibSen sensors for in-line monitoring the resin curing process, and therefore to provide a simple method for real-time quality assurance of composite manufacturing. In particular, the SWCNT-FibSen sensors are able to provide the local curing information in the interior of the laminated prepregs, which cannot be accessed readily by other commonly used techniques for this purpose, e.g.,

differential scanning calorimetry (DSC), dynamic mechanical analysis (DMA), infrared spectroscopy (IRS), optical and dielectric spectroscopy [33, 88].

4.4.3 In-situ structural health monitoring of polymeric composites

4.4.3.1 Coupled electrical – cyclic tension, bending, and compression tests

As demonstrated previously, the resistance change of SWCNT-FibSen sensor provides useful resin curing information during the composite manufacturing process. On the other hand, the same embedded sensor can also be used as the piezoresistive or strain sensor for monitoring the mechanical loading/deformation of the host composite structures. Figure 20a shows the coupled electrical-cyclic tensile testing results for a stand-alone glass SWCNT-FibSen sensor.

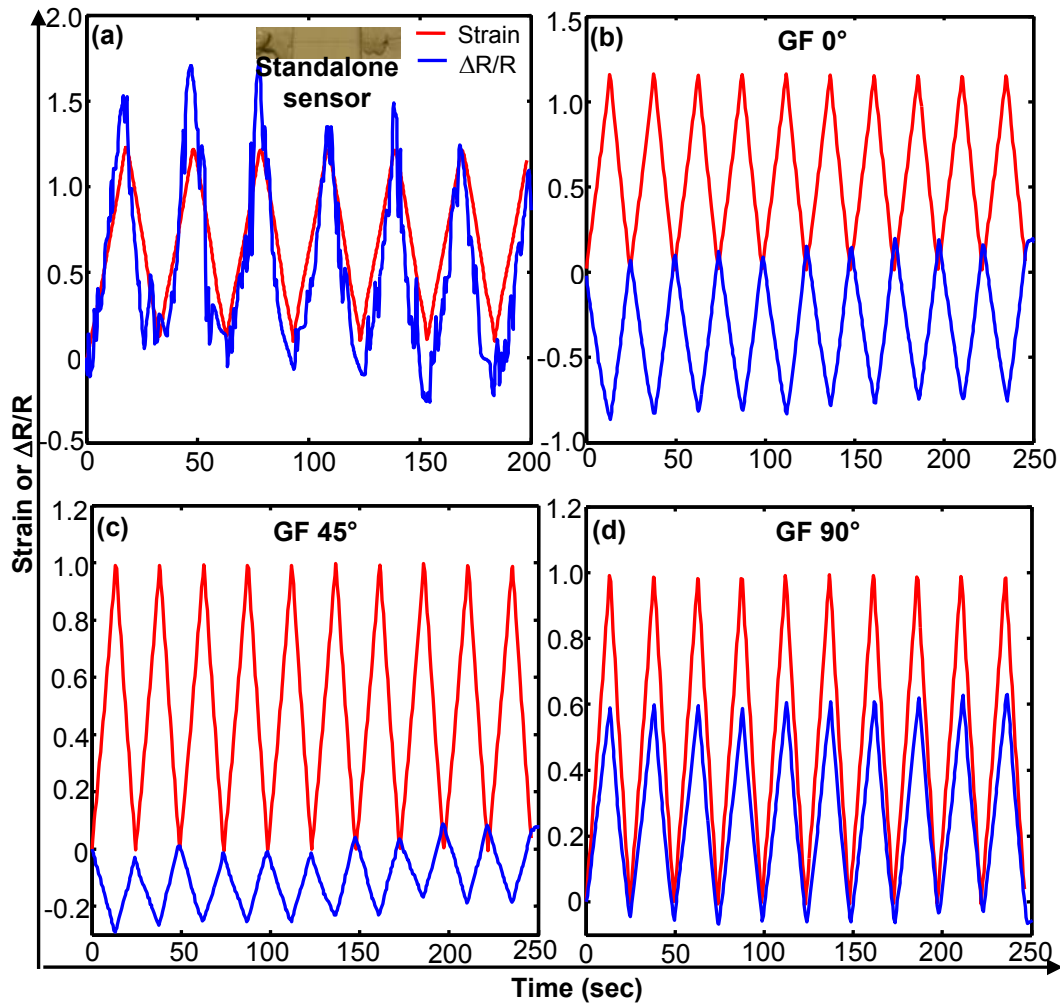


Figure 20. Piezoresistive response of the representative SWCNT-FibSen sensor under cyclic tensile test. (a) standalone sensor with glass fiber as the substrate; Inset photo in (a) shows that two ends of the neat fiber sensor was fixed onto two separate cardboard using instant adhesive before mounting on DMA. (b), (c) and (d) Glass SWCNT-FibSen sensors embedded in epoxy/glass fiber laminate and oriented at 0°, 45°, and 90° respectively with respect to the tensile loading direction.

Given the noisy signal that was attributed to the experimental difficulty in handling small sample size (a single glass fiber filament of diameter 20 μm), the linear piezoresistive behavior of the SWCNT-FibSen sensor is apparent. The sensor resistance is linearly proportional to the applied tensile strain; the higher the tensile strain, the higher is the sensor resistance. The gauge factor (GF) of the sensor was evaluated to be 1.25 ± 0.16 . The stand-alone SWCNT-FibSen sensor shows similar/comparable piezoresistive behavior as the large-area SWCNT thin films sprayed coated on a 2D PET substrate as reported in our previous studies [31]. In contrast to the stand-alone sensor, the embedded SWCNT-FibSen sensor subjected to three-stage curing and thermal-aging process show drastically different piezoresistive behavior. Figure 20b shows the coupled electrical-cyclic tensile testing results for a glass SWCNT-FibSen sensor embedded in a fully cured epoxy/glass fiber laminate coupon sample. During the test, the tensile load was applied to the laminate coupon in the direction of the fiber axis of the SWCNT-FibSen sensor. Clearly, the embedded sensor shows negative piezoresistivity with GF evaluated as -0.81 ± 0.03 . The sensor resistance decreases with increasing the tensile strain. The negative piezoresistivity of the embedded SWCNT-FibSen sensor can be understood within the framework of tunneling effect as a critical factor to dictate the piezoresistive response of CNT/polymer nanocomposites.

The negative piezoresistivity of the embedded SWCNT-FibSen sensor can be understood within the framework that the electrical resistance of CNT nanocomposite is dominated by the tunneling resistance rather than the intrinsic resistance of the CNTs. When the nanocomposite is under tension (compression), its resistance would increase (decrease) due to the enlarged separation and the correspondingly increased (decreased) tunneling resistance between the neighboring CNTs in the polymer matrix. As discussed previously, when the embedded SWCNT-FibSen sensor is subjected to the curing process, the resin molecules can penetrate/infiltrate into the SWCNT network. This effectively transforms the neat SWCNT thin film into a SWCNT/polymer nanocomposite system. As a result, one expects that the tunneling-effect dominated piezoresistive mechanism can also be applied to understand the piezoresistive behavior of the embedded SWCNT-FibSen sensors. With a consideration of the tunneling effect as well as the Poisson effect of the epoxy/glass fiber laminate [87], the negative piezoresistivity of the embedded SWCNT-FibSen sensor observed in Figure 20b can be well explained. When the laminate is tensioned along the fiber axis direction of the sensor, its transverse direction is subjected to compression. These two different deformation modes induce mechanical loading to the fiber sensor respectively in the longitudinal and transverse direction. The longitudinal loading transferred to the fiber sensor by the laminate tension is through the shear deformation of the resin matrix; and the transverse loading is a direct result of the laminate compression. For this reason and a presumed low efficiency of the load transfer in the longitudinal direction, one expects the resistance change of the embedded SWCNT-FibSen sensor is dominated by the transverse compression. As a result of the compression, the inter-tube distance is reduced to cause a decrease of the tunneling resistance in the SWCNT network and therefore to manifest the embedded SWCNT-FibSen sensor with negative piezoresistivity. To further verify this idea, the coupled electrical-cyclic tensile test was also applied to the coupons of epoxy/glass fiber laminate in which the fiber sensor was oriented at 45° and 90° with respect to the tensile loading direction. The results are shown in Figure 20c and 20d

respectively. In accordance to the Poisson effect explanation as suggested previously, the fiber sensor oriented at 90° shows positive piezoresistivity ($GF = 0.66 \pm 0.03$). The positive piezoresistivity for the 90° sensor is attributed to that the transverse direction of the fiber sensor is subjected to tension, which causes an increase of the inter-tube distance and therefore an increase of the sensor resistance. It is now clear that, when the fiber sensor is in 0° degree orientation with respect to the external tension, its transverse direction is subjected to compression and the sensor shows negative piezoresistivity; and when the fiber sensor is in 90° degree orientation with respect to the external tension, its transverse direction is subjected to tension and the sensor shows positive piezoresistivity. Given this, one expects that the fiber sensor oriented at 45° with respect to the tension direction should show least piezoresistive response. This is indeed the case as shown in Figure 20c for the 45° oriented sensor, which shows significantly reduced piezoresistive sensitivity with GF of -0.25 ± 0.029 .

To test the long-term durability of the SWCNT-FibSen sensor, an epoxy/glass fiber laminate embedded with a 90° oriented glass fiber sensor was submitted to 10,000 cyclic tensile tests. During the test, the cyclic displacement with amplitude of 0.2 mm (corresponding strain of 1%) and rate of 1 mm/min (corresponding strain rate of 5 %/min) was applied to the laminate coupon. After 10,000 cycles, we observed a slight 1.2 % increase on the sensor resistance and a minor 3.7 % reduction of the gage sensitivity. The excellent durability of SWCNT-FibSen sensors warrants their future applications as embedded sensing elements for SHM of high-performance polymeric composite structures.

In addition to tension, we also explored the versatility of the embedded SWCNT-FibSen sensor for detecting other types of mechanical deformation of the host composites. Figure 21a shows the coupled electrical-cyclic three-point bending test results for a three-layer laminate specimen, in which two fiber sensors were embedded. One is positioned above the neutral surface and the other is positioned below the neutral surface. Clearly, the fiber sensor above the neutral surface, which is subjected to compression in the longitudinal direction and tension in the transverse direction, shows increased resistance. In contrast, the fiber sensor below the neutral surface, which is subjected to tension in the longitudinal direction and compression in the transverse direction, shows decreased resistance. The bending test results again corroborate the Poisson effect explanation for the piezoresistive response of embedded SWCNT-FibSen sensors. Similarly, the negative piezoresistivity of the embedded SWCNT-FibSen sensor was also observed in a cyclic compression test on a 2-layer laminate coupon as shown Figure 21b. In this case, the transverse direction of the fiber sensor is directly subjected to compression.

4.4.3.2 Tension-to-failure test

The tension, bending, and compression testing results shown previously all indicate that the embedded SWCNT-FibSen sensors are useful for detecting and mapping the strain and stress of the host composite at small deformation. To further explore the behavior of embedded SWCNT-FibSen sensor at large deformation, a 2-layer epoxy/glass fiber laminate embedded with a fiber sensor in 0° orientation was subjected to tensile test to failure. The results are shown in Figure 22. At small deformation ($< 1.2\%$), the host laminate presents a linear stress-strain relation which is captured faithfully by a linear decrease of the sensor

resistance. The negative piezoresistivity of the 0° orientated sensor at small deformation is an expected result due to the Poisson effect as explained previously. With further increasing the strain level, strain-softening is observed for the laminate when the strain is greater than 1.2 %. Namely, the tensile modulus of the laminate at strain greater than 1.2 % is less than that at strain less than 1.2%. In coincidence with the strain-softening transition, the piezoresistivity of fiber sensor changes from negative to positive response. The strain-softening of the laminate is attributed to the initiation and development of micro-cracks in the epoxy matrix and fiber delamination. As a result, the contacts between CNT tubes in SWCNT network of the fiber sensor are disrupted to cause the resistance increase and the corresponding positive piezoresistive response. When the strain is further increased to 5.1%, as shown in Figure 22, a sudden rise of the fiber sensor resistance signifies the failure of the laminate. The behavior of the embedded SWCNT-FibSen sensors at large deformation shown in Figure 22 expects to be highly valuable in SHM of high performance fiber reinforced composites for detecting the micro-crack initiation and growth at early stage of the damage to prevent catastrophic failure.

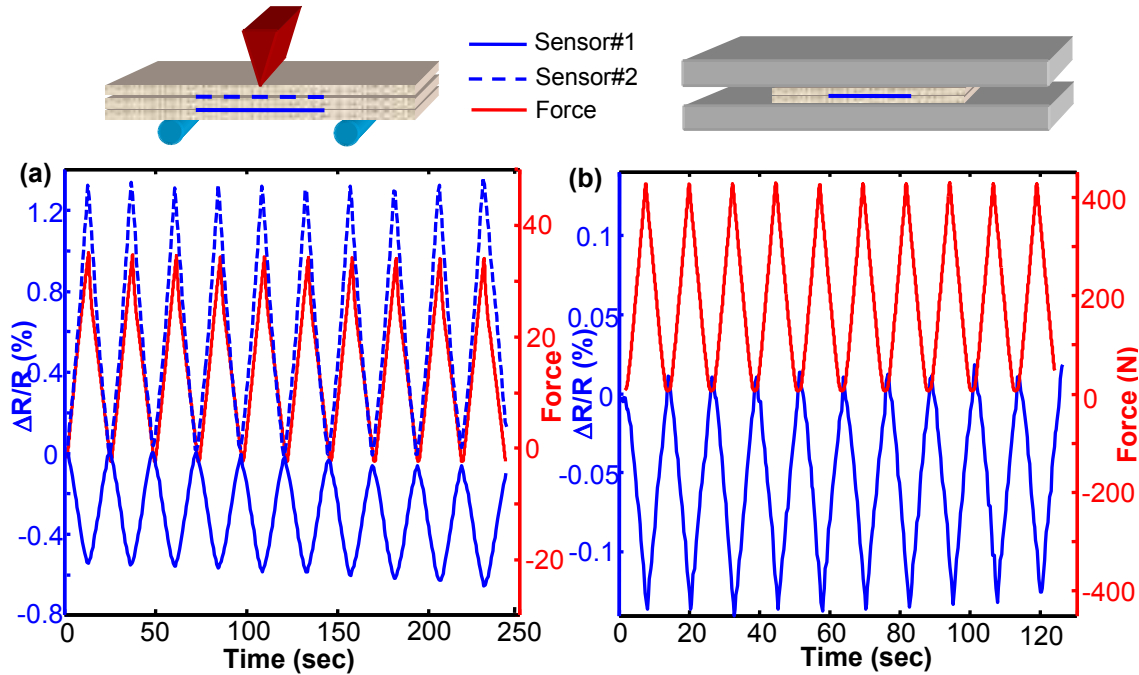


Figure 21. Piezoresistive response of glass SWCNTFibSen sensor embedded in epoxy/glass fiber laminate under (a) cyclic three-point bending test; and (b) cyclic compression test.

4.4.3.3 Simultaneous tensile tests of multiple SWCNT-FibSen sensors

SWCNT-FibSen sensors can be readily positioned and oriented in complex engineered composite systems for mapping the strain/stress and detecting the local damages. To demonstrate this idea, we fabricated a 2-layer epoxy/glass fiber laminate coupon with varied cross-section dimension, in which four glass fiber sensors were embedded at different positions and orientation angles (Figure 23).

As shown in Figure 23a, Sensor #1 is parallel to the long axis direction of the coupon with 0° orientation. Sensor #2 is oriented at 90° and located at the center position of the laminate with the smallest cross-section dimension of 8.5 mm. Sensor #3 and #3' have the same orientation as sensor #2, but they are respectively positioned ± 11.5 mm away from sensor #2, where the cross-section dimension is 14.5 mm. With a cyclic tensile loading applied along the long axis direction of the laminate coupon, the piezoresistive response of these four sensors was simultaneously recorded and the results are shown in Figure 23b. As expected, the 0°-oriented sensor #1 shows negative piezoresistivity; and the three 90°-oriented sensors (#2, #3, and #3') all exhibit positive piezoresistivity. As compared to sensor #3 and #3', sensor #2 is located at the position with the smallest cross-section dimension. Consequently, sensor #2 expects to experience greater stress than sensor #3 and #3'. These stress variations have been nicely registered by the larger resistance increase of sensor #3 and #3' than that of sensor #2. Moreover, due to their symmetric arrangements about sensor #2, the equal stress state of sensor #3 and #3' has also been recorded by their identical resistance changes.

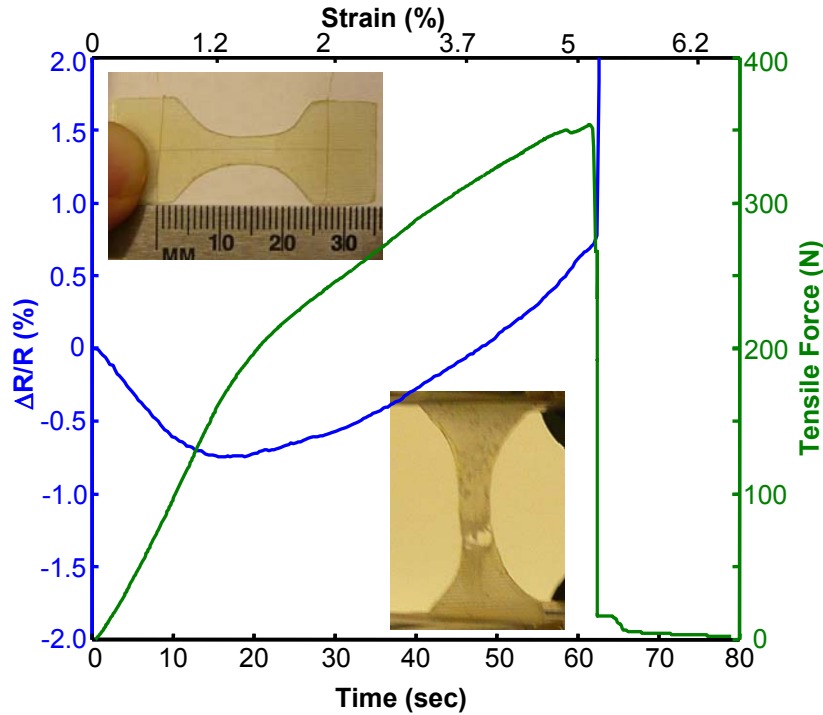


Figure 22. Piezoresistive response of glass SWCNT-FibSen sensor embedded in a 2-layer epoxy/glass fiber laminate that is subjected to tensile-to-failure test. Insets are the optical photographs of the dog-bone shaped laminate before and after the test.

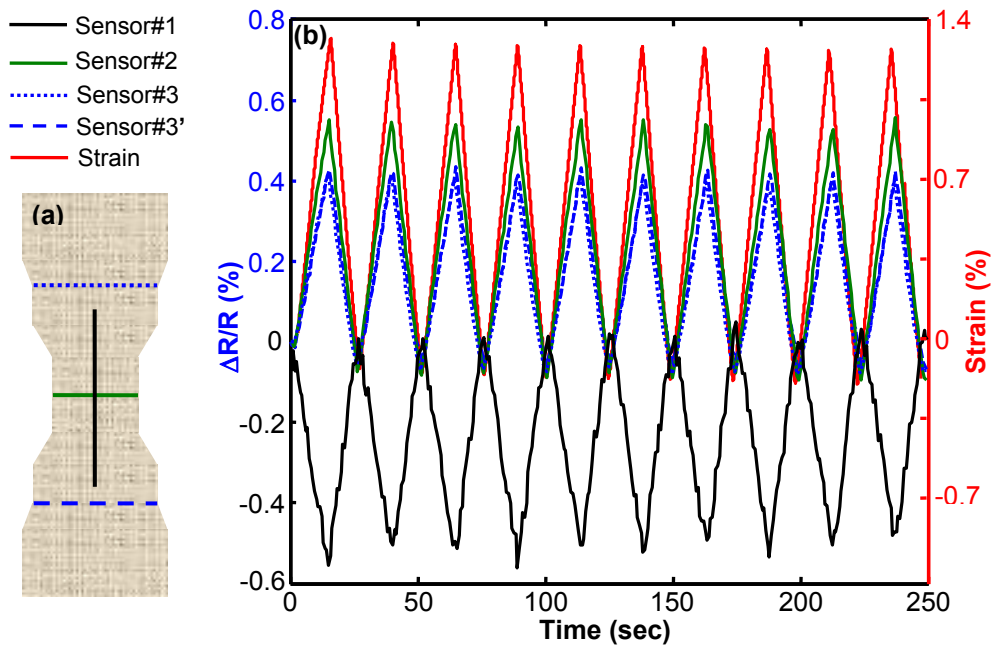


Figure 23. (a) Schematics of a 2-layer epoxy/glass fiber laminate embedded with multiple glass SWCNT-FibSen sensors. Sensor #1: 0° orientation; Sensor #2: 90° orientation and positioned at the center position of the laminate with the smallest cross-section dimension (8.5 mm); Sensor #3 and #3': 90° orientation and positioned ± 11.5 mm away from sensor #2. (b) Piezoresistive of Sensor #1, #2, #3 and #3' under when the epoxy/glass fiber laminate host is under cyclic tensile loading.

4.5 Graphite nanoplatelet enabled fiber sensor with dual functionalities for realization of multifunctional polymeric composites

The similar concept of SWCNT-FibSen can be equally applied to develop graphite nanoplatelet enabled fiber sensors – GNP-FibSen. With the roll-to-roll continuous spray coating process, GNP-FibSen sensors were fabricated by depositing GNP thin film on a single filament of glass fiber. Figure 24a shows the optical photograph of a GNP-FibSen. Further examination of the GNP-FibSen by SEM imaging shows a smooth glass fiber (Figure 24b) coated by an undulated GNP coating (Figure 24c), in which GNP platelets closely packed into a stacked mosaic structure (Figure 24d). The Raman scattering spectrum of the GNP-FibSen acquired with a 488 nm excitation laser is shown in Figure 24e. The signature Raman features [89,90,91] – D-band at 1361 cm^{-1} , G-band at 1581 cm^{-1} and the two-component 2D-band around 2730 cm^{-1} confirm the graphite nanoplatelet structures of the GNP-FibSen. Similar to SWCNT-FibSen, the GNP-FibSen sensor can also be easily embedded and integrated into the composite structures at desired locations and orientations during the manufacturing process to monitor the polymer resin curing process. An epoxy/fiberglass laminate sample embedded with a GNP-FibSen sensor was prepared to demonstrate this point. The result is shown in Figure 25.

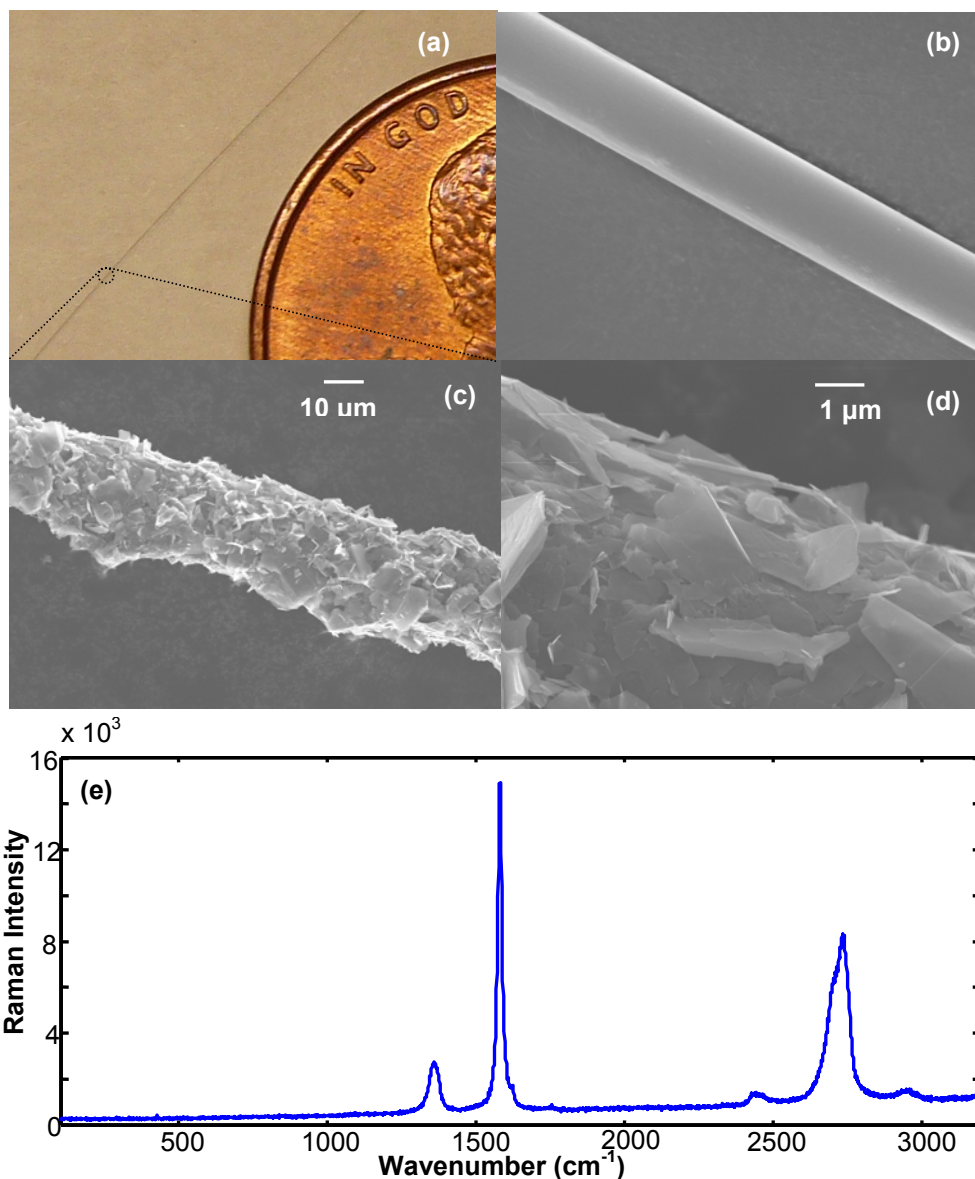


Figure 24. (a) Optical photograph of a neat GNP-FibSen sensor; (b) SEM image of a single filament of glass fiber used as the substrate for fabricating GNP-FibSen; (c) and (d) SEM images of the GNP packing structure in GNP-FibSen sensor; (e) Raman scattering spectrum of the neat GNP-FibSen.

As shown in Figure 25, the sensor resistance rapidly increases from 199.7 k Ω to 572.1 k Ω in the first stage of the curing process when the temperature ramps from 25 $^{\circ}\text{C}$ to 143 $^{\circ}\text{C}$. The resistance change is as high as $\sim 186\%$ during this stage. In the subsequent second stage of the curing process, during which the sample was maintained isothermally at 143 $^{\circ}\text{C}$, the sensor resistance initially manifests a rapid decrease from 572.1 k Ω to 466.1 k Ω and then gradually reaches a constant value of 403.6 k Ω . The overall change of the resistance during the second curing stage is $\sim -29.5\%$. The temperature-dependent resistance change of the embedded GNP-FibSen observed in Figure 25 is attributed to the progressive changes of the viscosity and crosslink density of the epoxy resin matrix during the curing process. In the first

stage of the curing process, the resin viscosity decreases with the rapid increase of the temperature from 25 °C to 143 °C. As a consequence, the resin monomers and oligomers can readily penetrate and infiltrate into the GNP network to cause a large separation and even breakage of GNP-GNP contacts, which therefore induces a significant resistance increase of the GNP-FibSen. In the subsequent isothermal stage of the curing process, the extent of the curing reaction and thus the crosslink density of the resin matrix keep increase. This induces a significant increase of the resin viscosity and the shrinkage of the resin matrix. As a result, the separation between GNP-GNP contacts is reduced to cause a decrease of the sensor resistance as observed in the beginning of the second stage of the curing process. With further increasing the cross-linking reaction, the system reaches a maximum shrinkage to cause the sensor resistance stabilized at a constant value. To further corroborate the aforementioned arguments, an epoxy/fiberglass laminate sample embedded with a carbon fiber filament was prepared and tested for its resistance response to the two-stage curing protocols. The rationale for selecting carbon fiber is due to that it has a similar but more densely packed graphitic platelet structures as GNP-FibSen [92]. Unlike the loosely packed GNP network in GNP-FibSen, the densely packed graphitic structures of the carbon fiber should not to be interrupted by the physical/chemical changes of the resin matrix in the curing process. As a consequence, we expect the resistance change of the carbon fiber in the curing process is simply due to the temperature effect. This is indeed the case as shown in Figure 25. In the first stage of the curing process, the carbon fiber shows a NTC (negative temperature coefficient of resistance) effect as the temperature ramps from 25 °C to 143 °C. This NTC behavior is an intrinsic electronic property of carbon fibers [93,94]. As expected, in the second stage of the curing process, the resistance of the carbon fiber maintains a constant, since the temperature is isothermally kept at 143 °C. The comparative studies shown in Figure 25 demonstrate the unique capability of the GNP-FibSen in providing the valuable information regarding the local physical/chemical changes of the resin matrix during the curing process.

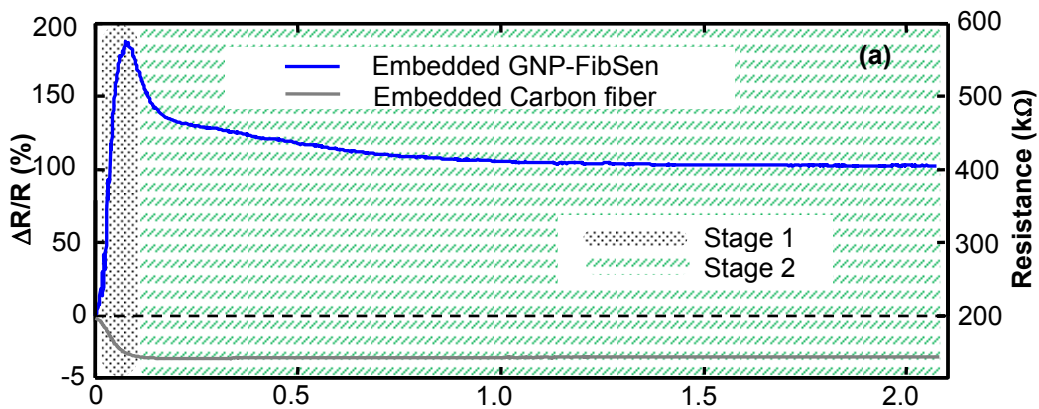


Figure 25. Two-stage curing process induced sensor resistance change for the embedded GNP-FibSen sensor and carbon fiber (CF). Stage 1 - temperature ramping from 25 °C to 143 °C; Stage 2 - isothermal at 143 °C for 2 hrs.

By applying the cyclic tensile strain of 1% in amplitude to the fully cured epoxy/fiberglass laminate (Figure 26a), the piezoresistivity of the embedded GNP-FibSen sensor

was evaluated. Figure 26b shows the results of the sensor resistance at different cyclic frequencies (0.04 Hz to 0.67 Hz). Clearly, the sensor response to the external deformation is instant and shows no frequency dependence. Figure 26c summarizes the GF of the embedded GNP-FibSen sensor tested at different cyclic frequencies. Averaged over the results obtained at different cyclic frequencies, the embedded GNP-FibSen sensor gives a $GF = 2.42 \pm 0.11$. As compared to the standalone sensor ($GF = 17.0 \pm 1.3$), one notes the embedded sensor has a significantly reduced sensitivity. The well-known Poisson effect is believed to be responsible, at least partially, for this phenomenon. As the laminate is under tension in the longitudinal direction of the embedded GNP-FibSen sensor, the transverse direction of the sensor is subjected to compression. The tension causes the sensor resistance increase by increasing the inter-particle (GNPs) distance; and the compression induces a decrease of the sensor resistance by decreasing the inter-particle (GNPs) distance. These two opposite effects act simultaneously to result in a smaller sensor resistance change and therefore a reduced GF as compared to the standalone GNP-FibSen. The indirect evidence to support this explanation may be found from Hu et al.'s work [41] on the piezoresistivity of polymer/carbon nanotube composite strain sensor. When the sensor is under tension, the resistance increases; and when the sensor is under compression, the resistance decreases. Certainly, the different nature of the GNP-GNP contacts in the standalone and the embedded sensors may also play a role regarding their significantly different gauge sensitivity. In the standalone sensor, there is a direct GNP-GNP contact; but in the embedded sensor, there is very likely an insulating layer of resin molecules to modulate the GNP-GNP contacts. As a consequence, one may expect the different mechanical as well as electrical response for the standalone and the embedded sensors and therefore their piezoresistive response. To evaluate the durability of the embedded GNP-FibSen sensor, the epoxy/glass fiber laminate sample was subjected to a coupled electrical-mechanical test with 10,000 cycles of cyclic tensile loading (1% in amplitude at a cyclic frequency of 0.08 Hz). Figure 26d shows the sensor resistance recorded for the first and last 100 cycles. Further calculation indicated that, for the first 100 cycles, the sensor resistance at 0% strain has an average value of $513.5 \pm 0.3 \text{ k}\Omega$ and the averaged GF is 2.40 ± 0.09 ; for the last 100 cycles, the sensor resistance at 0% strain has an average value of $513.5 \pm 0.2 \text{ k}\Omega$ and the averaged GF is 2.34 ± 0.06 . The minor changes of the sensor resistance and the GF after 10,000 cyclic tensile tests manifest the excellent durability of the embedded GNP-FibSen sensor, which warrants its future application as a reliable sensing system in SHM of high-performance polymeric composite structures.

GNP-FibSen sensors can be easily and non-invasively integrated into a complex shaped composite structure at desired orientations and locations for mapping the strain/stress and detecting the local damages. To demonstrate this point, a 3-layer epoxy/glass fiber laminate with a curved shape was fabricated and embedded with two GNP-FibSen sensors for sensing different deformation modes. Figure 27a shows the optical graph of the fabricated part. Figure 27b schematically shows the position of the embedded sensors: one (Sa) is positioned above and the other (Sb) is positioned below the neutral surface. Figure 27c shows the resistance change respectively recorded for both Sa and Sb when the part was subjected to repeat bending deformation by compressing its two ends manually. In such a deformation mode, Sa is under tension and Sb is under compression. It is noted that, due to the instrumentation limit,

the resistance for Sa and Sb were not measured synchronously but separately. This results in the not-in-phase response of Sa and Sb as shown in Figure 27c. Given this limitation, one still can identify that the different deformation modes experienced by Sa and Sb have been nicely captured by their respective resistance changes. That is, while the part was under compression, the resistance of Sa increased and the resistance of Sb decreased. When the part was in a free state, the resistance of both sensors recovered to their original values.

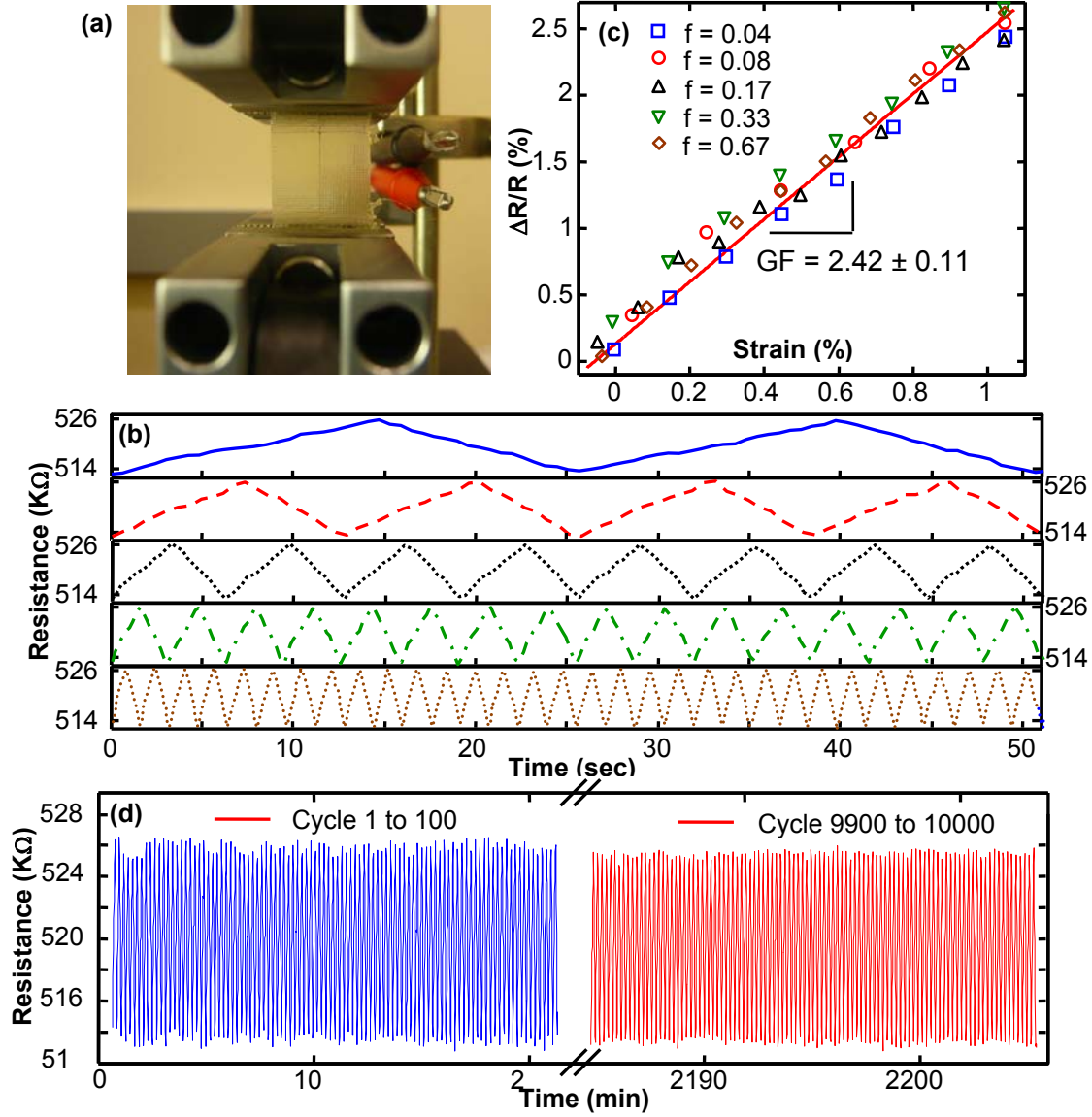


Figure 26. (a) Shimadzu mechanical setup for testing the piezoresistive performance of a GNP-FibSen sensor embedded in fully cured epoxy/glass fiber composites; The piezoresistive response (b) and gauge factor (c) of the embedded fiber sensor under cyclic tensile deformation at various frequencies (from top to bottom: 0.04, 0.08, 0.17, 0.33, 0.67 Hz); (d) Durability test results of the embedded fiber sensor subjected to 10,000 cycles of cyclic tensile test. The blue line is the results for the first 100 cycles and the red line is for the last 100 cycles.

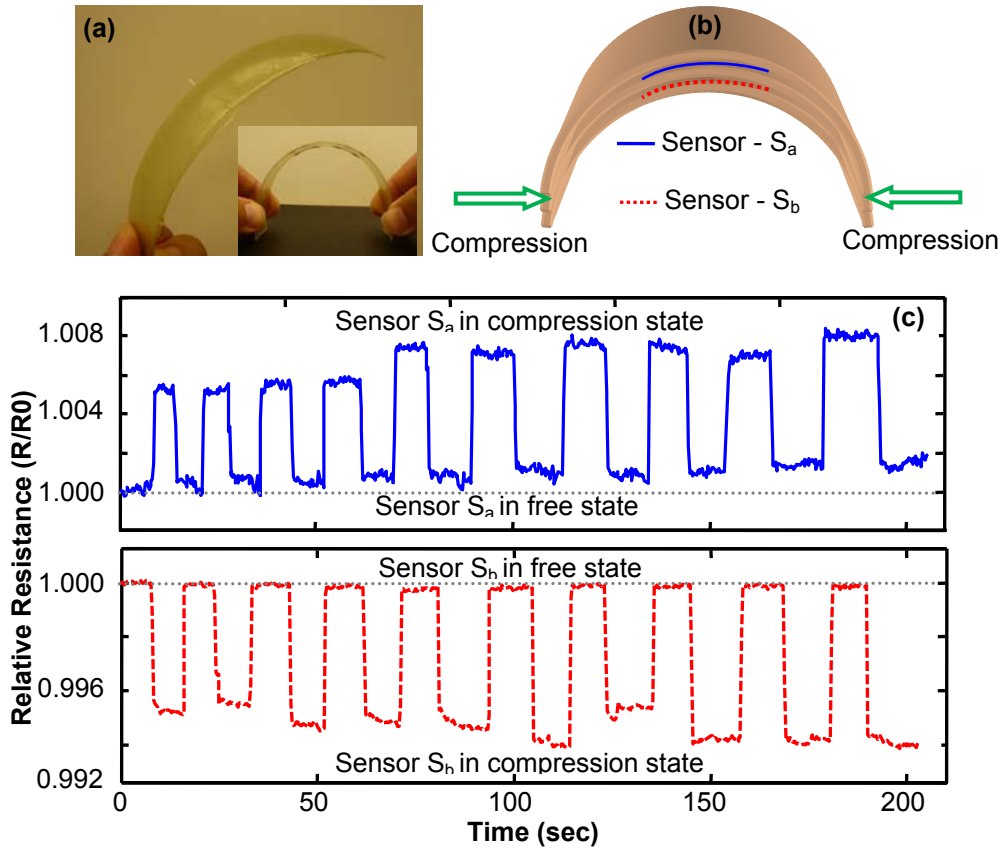


Figure 27. (a) Photo images and (b) schematics of the contour shaped composite laminates embedded with two GNP-FibSen sensors; S_a and S_b are respectively positioned above and below the neutral surface. (c) Resistance response of S_a and S_b when the part is subjected to repeating bending deformation by compressing its two ends manually.

5. Conclusion

Carbon nanomaterials, including single-walled carbon nanotubes (SWCNTs) and graphite nanoplatelets (GNPs), enabled fiber sensors - SWCNT-FibSen and GNP-FibSen are developed. The fabrication of SWCNT-FibSen and GNP-FibSen is simple, cost-effective, and environmental benign. They take a continuous fiber form and can be non-invasively and easily embedded into polymeric composite structures at the desired locations and orientations. The SWCNT-FibSen and GNP-FibSen sensors possess multipurpose sensing capabilities. In the composite manufacturing process, the resin curing process can be monitored to provide valuable quality assurance information; and after the composite manufacturing process, the same embedded sensors are capable of detecting/mapping different mechanical deformation modes - tension, bending, and compression as well as the failure of the host structure. Moreover, the fundamental research efforts lead to a series of easy-to-use and reliable methods for quantitatively characterizing the structures of carbon nanomaterials in the dispersion, which allows for establishing the processing-structure-property relationships of SWCNT-FibSen and GNP-FibSen sensors and paves the way for their large-scale production and deployment in

monitoring the health states of high-performance polymeric composite structures. To materialize and mature the SWCNT-FibSen and GNP-FibSen technology, the future research should focus on addressing the following issues: 1) development of simulation and modeling tools for better design and optimize the sensing performance; 2) exploration and development of a miniaturized, onboard and wireless sensing, power and communication systems; and 3) development of passivating/insulating/packaging methods to allow for their use in the SHM of electrically conducting high-performance polymeric composite structures, e.g., carbon fiber reinforced composites.

6. References

- [1] Boller C, Chang F, Fujino Y. Encyclopedia of Structural Health Monitoring. Hoboken NJ: Wiley; 2009.
- [2] Chang F. Structural health monitoring 2013 – a Roadmap to intelligent structures. Lancaster PA: DEStech Publications Inc; 2013.
- [3] Window AL, Holister GS. Strain gauge technology. 2nd ed. New York NY: Elsevier Science Publishers Ltd; 1992.
- [4] Moletn L, Aktepe B. Review of fatigue monitoring of agile military aircraft. Fatigue Fract. Eng. Mater. Struct. 2000; 23:767-785.
- [5] Kessler SS, Spearing SM, Soutis C. Damage detection in composite materials using lamb wave methods. Smart Mater. Struct. 2002; 11:269-278.
- [6] Qing X, Beard SJ, Kumar A, Ooi TK, Chang F. Built-in sensor network for structural health monitoring of composite structure. J. Int. Mat. Sys. Struc. 2007; 18:39-49.
- [7] Takeda N. Summary report of the structural health-monitoring project for smart composite structure systems. Adv. Comp. Mat. 2001; 10:107-118.
- [8] Kister G, Wang L, Ralph B, Fernando GF. Self-sensing E-glass fibers. Opt. Mat. 2003; 21:713-727.
- [9] Lee B. Review of the present status of optical fiber sensors. Opt. Fiber. Tech. 2003; 9:57-79.
- [10] Culshaw B. Optical fiber sensor technologies: opportunities and perhaps pitfalls. J. Lightwave Tech. 2004; 22:39-50.
- [11] Placko D, Dufour I. A focused-field eddy current sensor for nondestructive testing. IEEE Trans. Mag. 1993; 29:3192-3194.
- [12] Sadler DJ, Ahn CH. On chip eddy current sensor for proximity sensing and crack detection. Sensor Actuator 2001; 91:340-345.
- [13] Kannan E, Maxfield BW, Balasubramaniam K. SHM of pipes using torsional waves generated by in situ magnetostrictive tapes. Smart Mater. Struct. 2007; 16:2505-2515.

-
- [14] Grow RJ, Wang Q, Cao J, Wang DW, Dai HJ. Piezoresistance of carbon nanotubes on deformable thin-film membranes. *Appl. Phys. Lett.* 2005; 86:93104-3107.
- [15] Stampfer C, Jungen A, Linderman R, Obergfell D, Roth S, Hierold C. Nano-electromechanical displacement sensing based on single-walled carbon nanotubes. *Nano Lett.* 2006; 6:1449-453.
- [16] Minot ED, Yaish Y, Sazonova V, Park JY, Brink M, McEuen PL. Tuning carbon nanotube band gaps with strain. *Phys. Rev. Lett.* 2003; 90:156401.
- [17] Cao J, Wang Q, Dai H. Electromechanical Properties of Metallic, Quasimetallic, and Semiconducting Carbon Nanotubes under Stretching. *Phys. Rev. Lett.* 2003; 90:157601.
- [18] Kang I, Schulz MJ, Kim JH, Shanov V, Shi D. A carbon nanotube strain sensor for structural health monitoring. *Smart Mater. Struct.* 2006; 15:737-748.
- [19] Loh KJ, Kim J, Lynch JP, Kam NWS, Kotov NA. Multifunctional layer-by-layer carbon nanotube-polyelectrolyte thin films for strain and corrosion sensing. *Smart Mater. Struct.* 2007; 16:429-438.
- [20] Rein MD, Breuer O, Wagner HD. Sensors and sensitivity: carbon nanotube buckypaper films as strain sensing devices. *Compos. Sci. Technol.* 2011; 71:373-381.
- [21] Thostenson ET, Chou TW. Real-time in situ sensing of damage evolution in advanced fiber composites using carbon nanotube networks. *Nanotechnology* 2008; 19:215713.
- [22] Thostenson ET, Chou TW. Carbon nanotube networks: sensing of distributed strain and damage for life prediction and self healing. *Adv. Mater.* 2006; 18:2837-2841.
- [23] Gao L, Thostenson ET, Zhang Z, Chou TW. Sensing of damage mechanisms in fiber-reinforced composites under cyclic loading using carbon nanotubes. *Adv. Funct. Mater.* 2009; 19:123-130.
- [24] Zhao H, Zhang Y, Bradford PD, Zhou Q, Jia Q, Yuan F, et al. Carbon nanotube yarn strain sensors. *Nanotechnology* 2010; 21:305502.
- [25] Abot JL, Song Y, Vatsavaya MS, Medikonda S, Kier Z, Jayasinghe C, et al. Delamination detection with carbon nanotube thread in self-sensing composite materials. *Compos. Sci. Tech.* 2010; 70:1113-1119.
- [26] Sebastian J, Schehl N, Bouchard M, Boehle M, Li L, Lagounov A, et al. Health monitoring of structural composites with embedded carbon nanotube coated glass fiber sensors. *Carbon* 2014; 66: 191-200.
- [27] Zhang J, Liu J, Zhuang R, Mader E, Heinrich G, Gao S. Single MWNT-glass fiber as strain sensor and switch. *Adv. Mater.* 2011; 23:3392-3397.
- [28] Kessler SS. Piezoelectric-based in-situ damage detection of composite materials for structural health monitoring systems. Ph.D. Thesis, MIT, Cambridge, Massachusetts (2002)

-
- [29] Marantidis C, Van Way CB, Kudva JN. Acoustic-Emission Sensing in an On-Board Smart Structural Health Monitoring System for Military Aircraft. *Proceedings of the SPIE Conference on Smart Structures and Integrated Systems*. 1994; 2191:258-264.
- [30] Boller C. Next generation structural health monitoring and its integration into aircraft design. *Int. J. Sys. Sci.* 2000; 31:1333-1349
- [31] Luo S, Liu T. Structure-property-processing relationships of single-wall carbon nanotube thin film piezoresistive sensors. *Carbon* 2013; 59:315-324.
- [32] Luo S, Liu T. SWCNT/graphite nanoplatelet hybrid thin films for self-temperature-compensated, highly sensitive, and extensible piezoresistive sensors. *Adv. Mater.* 2013; 25:5650-5657.
- [33] Hayaty M, Beheshty MH, Esfandeh M. Cure kinetics of a glass/epoxy prepreg by dynamic differential scanning calorimetry. *J. Appl. Poly. Sci.* 2011; 120:62-69.
- [34] Liu T, Luo S, Xiao Z, Zhang C, Wang B. Preparative ultracentrifuge method for characterization of carbon nanotube dispersions. *J. Phys. Chem. C* 2008; 112:19193-19202.
- [35] Liu T, Xiao Z. Exact and Closed Form Solutions for the Quantum Yield, Exciton Diffusion Length, and Lifetime To Reveal the Universal Behaviors of the Photoluminescence of Defective Single-Walled Carbon Nanotubes. *J. Phys. Chem. C*, 2011; 115:16920-16927.
- [36] Yao Y, Luo S, Liu T. Determination of the Length, Diameter, Molecular Mass, Density and Surfactant Adsorption of SWCNTs in Dilute Dispersion by Intrinsic Viscosity, Sedimentation, and Diffusion Measurements. *Macromolecules*, 2014; 47:3093-3100.
- [37] Obitayo W, Luo S, Xiao Z, Liu T, Guan J. Gel electrophoresis and Raman mapping for determining the length distribution of SWCNTs. *RSC Adv.*, 2014; 4:37070-37078.
- [38] Liu T, Xiao Z. Dynamic Light Scattering of Rigid Rods – A Universal Relationship on the Apparent Diffusion Coefficient as Revealed by Numerical Studies and Its Use for Rod Length Determination. *Macromol. Chem. Phys.* 2012, 213, 1697 – 1705.
- [39] Rahman R, Servati P. Effects of inter-tube distance and alignment on tunnelling resistance and strain sensitivity of nanotube/polymer composite films. *Nanotechnology*, 2012; 23:055703.
- [40] Wang Z, Ye X. A numerical investigation on piezoresistive behaviour of carbon nanotube/polymer composites: mechanism and optimizing principle. *Nanotechnology*, 2013; 24:265704.
- [41] Hu N, Karube Y, Arai M, Watanabe T, Yan C, Li Y, Liu Y, Fukunaga H. Investigation on sensitivity of a polymer/carbon nanotube composite strain sensor. *Carbon*, 2010; 48:680-687.
- [42] Theodosiou TC, Saravanos DA. Numerical investigation of mechanisms affecting the piezoresistive properties of CNT-doped polymers using multi-scale models. *Comp. Sci. Tech.*, 2010; 70:1312-1320.

-
- [43] Hu B, Hu N, Li Y, Akagi K, Yuan W, Watanabe T, Cai Y. Multi-scale numerical simulations on piezoresistivity of CNT/polymer nanocomposites, *Nanoscale Res. Lett.*, 2012; 7:1-11.
- [44] Liu T, Xiao Z, Wang B. The exfoliation of SWCNT bundles examined by simultaneous Raman scattering and photoluminescence spectroscopy. *Carbon*, 2009; 47:3529-3537.
- [45] Attal S, Thiruvengadathan R, Regev O. Determination of the Concentration of Single-Walled Carbon Nanotubes in Aqueous Dispersions Using UV-Visible Absorption Spectroscopy. *Anal. Chem.*, 2006; 78:8098-8104.
- [46] Mason M, Weaver W. The settling of small particles in a fluid. *Phys. Rev.*, 1924; 23:412-426.
- [47] Shiragami N, Kajiuchi TP. Precipitation of protein by ultracentrifuge with angle rotor. Part 1: Model for sedimentation process. *Bioproc. Eng.*, 1990; 5:85-88.
- [48] Kestin J, Sokolov M, Wakeham WA. Viscosity of liquid water in the range -8 °C to 150 °C. *J. Phys. Chem. Ref. Data*, 1978; 7:941-948.
- [49] Keithley Instruments, Inc. Low level measurements handbook. 6th ed. USA; 2004.
- [50] Liu T, Kumar S. Quantitative characterization of SWNT orientation by polarized Raman spectroscopy. *Chem. Phys. Lett.*, 2003; 378:257-262.
- [51] Teraoka I. *Polymer solutions: an introduction to physical properties*; John Wiley & Sons, Inc.: New York, 2002.
- [52] Doi M, Edwards SF. *The Theory of Polymer Dynamics*; Oxford University Press: Oxford, 1986.
- [53] Mansfield ML, Douglas JF. Transport Properties of Rodlike Particles. *Macromolecules*, 2008; 41:5422-5432.
- [54] Parra-Vasquez ANG, Stepanek I, Davis VA, Moore VC, Haroz EH, Shaver J, Hauge RH, Smalley RE, Pasquali M. Simple Length Determination of Single-Walled Carbon Nanotubes by Viscosity Measurements in Dilute Suspensions. *Macromolecules*, 2007; 40:4043-4047.
- [55] Tirado MM, Martinez CL, Delatorre JG. Comparison of theories for translational and rotational diffusion coefficients of rod-like macromolecules. Application to short DNA fragments. *J. Chem. Phys.*, 1984; 81:2047-2052.
- [56] Broersma S. Rotational diffusion constant of a cylindrical particle. *J. Chem. Phys.*, 1960; 32:1626-1631.
- [57] Yamakawa H. Viscoelastic Properties of Straight Cylindrical Macromolecules in Dilute Solution. *Macromolecules*, 1975; 8:339-342.
- [58] Matarredona O, Rhoads H, Li Z, Harwell JH, Balzano L, Resasco, DE. Dispersion of Single-Walled Carbon Nanotubes in Aqueous Solutions of the Anionic Surfactant NaDDBS. *J. Phys. Chem. B*, 2003; 107:13357-13367.

-
- [59] Király Z, Findenegg GH. Calorimetric Evidence of the Formation of Half-Cylindrical Aggregates of a Cationic Surfactant at the Graphite/Water Interface. *J. Phys. Chem. B*, 1998; 102:1203–1211.
- [60] Scamehorn JF, Schechter RS, Wade WH. Adsorption of surfactants on mineral oxide surfaces from aqueous solutions: I: Isomerically pure anionic surfactants. *J. Colloid Interf. Sci.*, 1982; 85:463–478.
- [61] Heller DA, et al. Concomitant Length and Diameter Separation of Single-Walled Carbon Nanotubes. *J. Amer. Chem. Soc.*, 2004; 126:14567-14573.
- [62] Elson E, Jovin TM. Fractionation of oligodeoxynucleotides by polyacrylamide gel electrophoresis. *Anal. Biochem.*, 1969; 27:193-204.
- [63] Elder JK, et al. Measurement of DNA length by gel electrophoresis: I. Improved accuracy of mobility measurements using a digital microdensitometer and computer processing. *Anal. Biochem.*, 1983; 128:223-226.
- [64] Kozulic B. Models of gel electrophoresis. *Anal. Biochem.*, 1995; 231:1-12.
- [65] Griess GA, et al. The sieving of rod-shaped viruses during agarose gel electrophoresis. I. Comparison with the sieving of spheres. *Biopolymers*, 1990; 29:1277-1287.
- [66] Fagan JA, et al. Length-Dependent Optical Effects in Single-Wall Carbon Nanotubes. *J. Amer. Chem. Soc.*, 2007; 129:10607-10612.
- [67] Hertel T, et al. Diffusion Limited Photoluminescence Quantum Yields in 1-D Semiconductors: Single-Wall Carbon Nanotubes. *ACS Nano*, 2010; 4:7161-7168.
- [68] Harrah DM, Swan AK. The Role of Length and Defects on Optical Quantum Efficiency and Exciton Decay Dynamics in Single-Walled Carbon Nanotubes. *ACS Nano*, 2010; 5:647-655.
- [69] Xiao Z, Gupta M, Baltas G, Liu T, Chae HG, Kumar S. Probe diffusion of SWCNTs in semidilute solutions of polyacrylonitrile homo- and copolymers: effects of topological constraints and polymer/nanorod interactions. *Polymer*, 2012; 53:5069-5077.
- [70] Wouterse A, Luding S, Philipse AP. On contact numbers in random rod packings. *Granu. Matt.*, 2009; 11:169–177.
- [71] Blouwolff J, Fraden S. The coordination number of granular cylinders. *Europhys. Lett.*, 2006; 76:1095-1101.
- [72] Philipse AP. The random contact equation and its implications for (colloidal) rods in packing, suspensions, and anisotropic powders. *Langmuir*, 1996; 12:1127-1133.
- [73] Hu N, Itoi T, Akagi T, Kojima T, Xue J, Yan C, et al. Ultrasensitive strain sensors made from metal-coated carbon nanofiller/epoxy composites. *Carbon*, 2013; 51:202-212.
- [74] Alamusi, Hu N, Fukunaga H, Atobe S, Liu Y, Li J. Piezoresistive strain sensors made from carbon nanotubes based polymer nanocomposites. *Sensors*, 2011; 11:10691-10723.

-
- [75] Parmar K, Mahmoodi M, Park C, Park SS. Effect of CNT alignment on the strain sensing capability of carbon nanotube composites, *Smart Mat. Struc.*, 2013; 22:075006.
- [76] Oliva-Avilés AI, Avilés F, Sosa V. Electrical and piezoresistive properties of multi-walled carbon nanotube/polymer composite films aligned by an electric field. *Carbon*, 2011; 49:2989-2997.
- [77] Schulgasser K. Fibre orientation in machine-made paper. *J. Mat. Sci.*, 1985; 20:859-866.
- [78] Lu W, Carlsson, LA. Micro-model of paper part 2: statistical analysis of the paper structure. *Tappi J.*, 1996; 79:203-210.
- [79] Sampson WW. Modeling stochastic fibrous materials with Mathematica, Springer-Verlag London Limited (2009).
- [80] Pallas-Areny R, Webster JG. *Sensors and Signal Conditioning*, 2nd ed., by John Wiley & Sons (2001).
- [81] Luo S, Liu T, Benjamin SM, Brooks JS. Variable range hopping in single-wall carbon nanotube thin films: a processing-structure-property relationship study. *Langmuir*, 2013; 29:8694-8702.
- [82] Skakalova V, Kaiser AB, Woo YS, Roth S. Electronic transport in carbon nanotubes: From individual nanotubes to thin and thick networks. *Phys. Rev. B*, 2006; 74:085403.
- [83] Kaiser AB, Skakalova V, Roth S. Modelling conduction in carbon nanotube networks with different thickness, chemical treatment and irradiation. *Physica E*, 2008; 40:2311 - 2318.
- [84] Dresselhaus MS, Dresselhaus G, Saito R, Jorio A. Raman spectroscopy of carbon nanotubes. *Phys. Rep.*, 2005; 409:47-99.
- [85] Wood JR, Zhao Q, Frogley MD, Meurs ER, Prins AD, Peijs T, et al. Carbon nanotubes: from molecular to macroscopic sensors. *Phys Rev B*, 2000; 62:7571-7575.
- [86] Venkateswaran UD, Brandsen EA, Schlecht U, Rao AM, Richter E, Loa I, et al. High pressure studies of the Raman-active phonons in carbon nanotubes. *Phys. Stat. Sol. b* 2001; 223:225-36.
- [87] Mallick PK. *Fiber-reinforced composites: materials, manufacturing, and design*. 3rd ed. New York NY: Marcel Dekker (2007).
- [88] Bang KG, Kwon JW, Lee DG, Lee JW. Measurement of the degree of cure of glass fiber-epoxy composites using dielectrometry. *J. Mater. Process. Tech.*, 2001;113:209-214.
- [89] Ferrari AC, Meyer JC, Scardaci V, Casiraghi C, Lazzeri M, Mauri F, Piscanec S, et al. Raman spectrum of graphene and graphene layers. *Phys. Rev. Lett.*, 2006; 97:187401.
- [90] Ferrari AC. Raman spectroscopy of graphene and graphite: disorder, electron-phonon coupling, doping and nonadiabatic effects. *Solid State Commun.*, 2007; 143:47-57.
- [91] Ferrari AC, Basko DM. Raman spectroscopy as a versatile tool for studying the properties of graphene. *Nat. Nanotech.*, 2013; 8:235-246.

[92] Harris PJF. New Perspectives on the Structure of Graphitic Carbons. *Crit. Rev. Solid State Mater. Sci.*, 2005; 30:235-253.

[93] Nysten B, Issi, J, Barton JR, Boyington DR, Lavin JG. Microstructure and Negative Magnetoresistance in Pitch-derived Carbon Fibers. *J. Phys. D*, 1991; 24:714-718.

[94] Donnet J, Wang TK, Rebouillat S, Peng JCM. *Carbon Fibers*, 3rd ed. Marcel Dekker: New York, NY (1998).